ARES I-X BEST ESTIMATED TRAJECTORY ANALYSIS AND RESULTS

Christopher D. Karlgaard
Analytical Mechanics Associates, Inc.
Hampton, VA

Roger E. Beck
Analytical Mechanics Associates, Inc.
Huntsville, AL

Brett R. Starr, Stephen D. Derry, and Jay M. Brandon
NASA Langley Research Center
Hampton, VA

Aaron D. Olds
Analytical Mechanics Associates, Inc.
Hampton, VA

ABSTRACT

The Ares I-X trajectory reconstruction produced best estimated trajectories of the flight test vehicle ascent through stage separation, and of the first and upper stage entries after separation. The trajectory reconstruction process combines on-board, ground-based, and atmospheric measurements to produce the trajectory estimates. The Ares I-X vehicle had a number of on-board and ground based sensors that were available, including inertial measurement units, radar, air-data, and weather balloons. However, due to problems with calibrations and/or data, not all of the sensor data were used. The trajectory estimate was generated using an Iterative Extended Kalman Filter algorithm, which is an industry standard processing algorithm for filtering and estimation applications. This paper describes the methodology and results of the trajectory reconstruction process, including flight data preprocessing and input uncertainties, trajectory estimation algorithms, output transformations, and comparisons with preflight predictions.

INTRODUCTION

The Ares I rocket was designed as part of NASA's Constellation Program to launch the Orion capsule containing 4 to 6 crew members to Low Earth Orbit (LEO) to support missions to the International Space Station, the moon, and beyond. A series of uncrewed test flights were planned to gather system performance data that cannot otherwise be obtained in ground testing. The first of these test flights, Ares I-X, occurred on October 28th, 2009.[1] A critical component to the performance evaluation of the Flight Test Vehicle (FTV) is the Best Estimated Trajectory (BET), which is reconstructed from all available flight data. The Ares I-X trajectory reconstruction produced best estimated trajectories of the flight test vehicle ascent through stage separation, and of the first and upper stage entries after separation. The trajectory reconstruction process combines on-board, ground-based, and atmospheric measurements to produce the trajectory estimates. These measurements arise from a number of on-board and ground based sensors, including inertial measurement units, radar, air-data, and weather balloons.

The BET was generated using an Iterative Extended Kalman Filter (IEKF) algorithm which is an industry standard processing algorithm for filtering and estimation applications. The IEKF algorithm is discussed in greater detail in later sections, but at a very high level, the algorithm amounts to a recursive weighted least-squares fit to all input data. Inputs to the BET filter consisted of data from on-board inertial measurement units, an on-board air data sensor, and radar at multiple ground tracking stations. Accelerations and angular rates from several inertial measurement units were integrated to provide an estimate of the vehicle state as a function of time. Tracking data from several ground-based radar stations and data

Approved for public release; distribution is unlimited.

from an on-board alpha/beta vane sensor were used as redundant observations and processed in the Kalman filter to improve the estimated state. Additionally, observations from balloon measurements were used to generate estimates of the atmospheric conditions on the day of flight. All these data sources were processed and used to generate the BET for the vehicle ascent trajectory until the expected loss of data due to First Stage (FS) and Upper Stage Simulator (USS) physical separation. After separation, the USS lost power due to the power supply being located on the FS and all of the sensors mounted on the USS became non operational. The first stage inertial measurement unit (IMU) continued to function during entry; thus, the IMU, radar, and atmospheric data were used to determine the FS entry BET. The USS entry trajectory was estimated using radar and atmospheric data alone and, as a result, only position and velocity of the USS entry were determined from separation through the loss of radar contact. After loss of radar contact, the remainder of the trajectory must be extrapolated using trajectory simulations.

SENSOR SUMMARY

The Ares I-X vehicle had a number of on-board and ground-based sensors that were available for the trajectory reconstruction process. However, due to problems with calibrations and/or data, not all of the sensor data were used. This section provides additional detail on the sensors. A summary of the sensors is given in Table 1.

Table 1: Ares I-X Sensor Summary

On-board Sensors		
	Inertial	Fault Tolerant Inertial Navigation Unit (FTINU)
		Forward Redundant Rate Gyro Unit (FRRGU)
		Aft Redundant Rate Gyro Unit (ARRGU)
		Space Integrated GPS/INS (SIGI)
	Air Data	5 Hole Probe
		Alpha/Beta Vanes
		Total Air Temperature
Ground-Based Sensors		Range Safety Radar (4)
		NASA Debris Radar
Meteorological Sensors		Low Resolution Flight Element (LRFE) Balloons
		High Resolution Flight Element (HRFE) Balloons

ON-BOARD SENSORS

Four on-board inertial sensors were available for use in trajectory reconstruction. These included the Fault Tolerant Inertial Navigation Unit (FTINU) on the USS, a Space Integrated Global Positioning System / Inertial Navigation System (SIGI) on the FS, and two Redundant Rate Gyro Units (RRGU), one on the USS and one on the FS. The location of these sensors is illustrated in Figure 1 and their X, Y, Z coordinates are listed in Table 2. The origin of this coordinate system is 152.16 inches forward of the vehicle structure. The FTINU and SIGI were both complete inertial measurement units in the sense that they provided 3-axis acceleration and angular rate measurements. The RRGU units provided measurements of pitch and yaw rates only. The trajectory reconstruction plan was to combine all available acceleration and angular rate data to improve the estimate of the FTV rigid body acceleration and rotation. Inertial acceleration was to be estimated from the combined FTINU and SIGI acceleration data, body pitch and yaw rates were to be estimated from the combined FTINU, SIGI, and RRGU's pitch and yaw data, and body roll rate was to be estimated from the combined FTINU and SIGI roll rate data. However, issues with the SIGI data quality during the ascent prevented its data from being used as planned in the ascent phase. This is discussed in more detail in later sections. After motor burnout, the SIGI data quality improved and it was used to reconstruct the FS entry.

Figure 2 illustrates the locations of the air data sensors installed on the CM/LAS structure. The air data sensors' X coordinates and clocking angles are listed in Table 3. The clock angle is measured clockwise

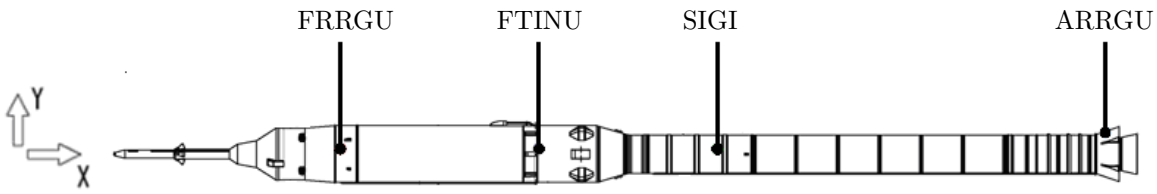

Figure 1: Ares I-X On-Board Inertial Sensors

Table 2: Inertial Sensor Locations

Sensor	X Coordinate (inch)	Y Coordinate (inch)	Z Coordinate (inch)
FRRGU	1023.8	-18.6	69.5
FTINU	1770.3	-5.72	60.0
SIGI	2476.8	41.39	-36.3
ARRGU	3962.9	58.0	33.5

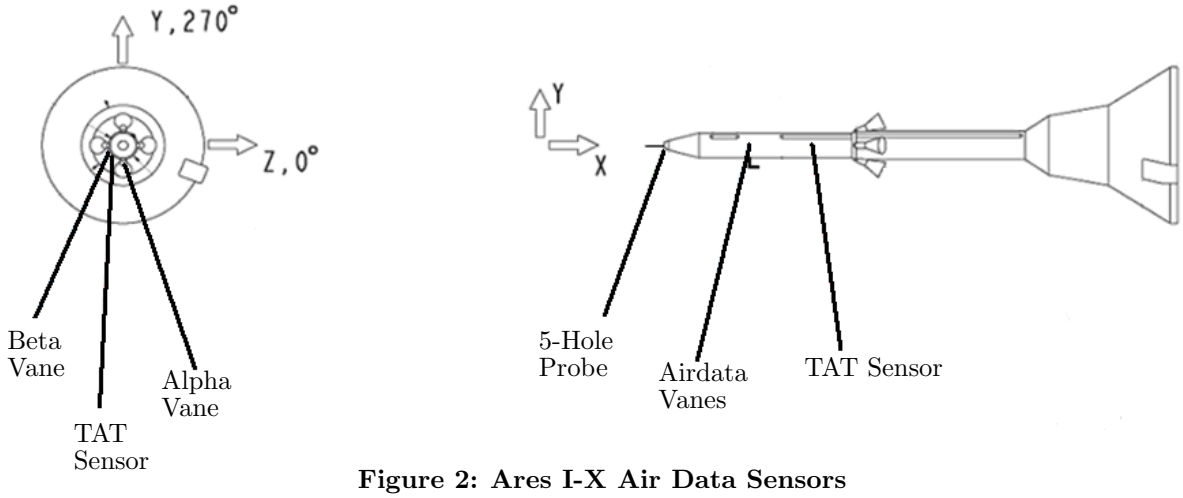

Figure 2: Ares I-X Air Data Sensors

from the Z axis looking from the top of the stack. These sensors consisted of a 5 hole probe, air data vanes, and a total air temperature (TAT) sensor. These measurements were designed to provide coupling between the free stream atmospheric states (winds, pressure, density, and temperature) and the vehicle inertial states (velocity and attitude). Specifically, the 5 hole probe was to provide angle of attack, angle of sideslip, and Mach number estimates, the air data vanes were to provide angle of attack and sideslip, and the total air temperature sensor was to provide a total temperature measurement. The preflight plan was to make use of all these sensors for trajectory reconstruction, however, data from the 5 hole probe and total air temperature sensors were not used in reconstruction. The 5 hole probe data was considered unreliable as a result of precipitation entering the holes prior to launch. As a result, it was recommended the data not be incorporated in the trajectory reconstruction. A complete description of the 5 hole probe calibration and precipitation contamination problems can be found in Reference 2. The total air temperature probe also had problems with its calibration. Its mount location was behind the shock wave and potentially in boundary layer flow requiring the development of a recovery factor as a function of Mach number. Wind tunnel tests with the TAT were conducted preflight and were to be used to determine the recovery factor. However, the Ares I Thermal Environment Panel that supported the test could not develop the recovery factor with uncertainties sufficiently small to improve the BET accuracy due to insufficient knowledge of the probe design and boundary layer height. As a result, the panel recommended the TAT data not be used in the trajectory reconstruction.

Table 3: Air Data Sensor Locations

Sensor	X Coordinate (inch)	Clock Angle (deg)
5 Hole Probe	152.2	0.0
Alpha Vane	256.0	90.0
Beta Vane	256.0	180.0
Total Air Temperature	334.0	135.0

GROUND-BASED SENSORS

Several C-band ground-based radar stations were used to track the vehicle during ascent and entry to provide range, azimuth, and elevation measurements primarily for range safety purposes but also for trajectory reconstruction purposes. These radar measurements consisted of beacon tracking data during ascent and skin tracking during entry. In addition, data was acquired from the NASA Debris Radar (NDR) for trajectory reconstruction purposes, consisting of one C-band tracking radar and two X-band Doppler radars mounted on the first stage recovery vessels. The specific ground-based radar stations locations are shown in Figure 3, along with an October nominal ascent and entry trajectory for comparison with the preflight predicted radar geometry.

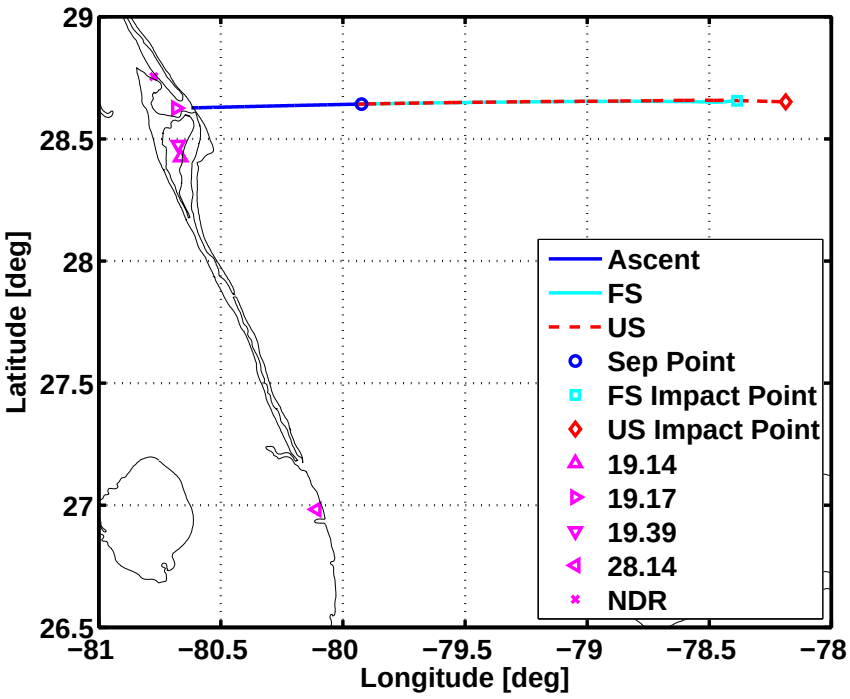

Figure 3: Ares I-X Ground-Based Radar Tracking Stations

Table 4 shows a summary of the radar designation numbers, type of radar, its location, and nominal accuracy numbers as provided by the Eastern Range for preflight BET accuracy assessments. NASA Debris Radar (NDR) data was acquired but was not used for trajectory reconstruction due to anomalies and discrepancies. In particular, the position and velocity time histories were inconsistent with the Range radar, and also no uncertainties were provided with the data in order to properly weight it in the Kalman filter. Radars 19.14, 19.17, 19.39, and 28.14 tracked the vehicle during ascent. After stage separation, radar 19.14 tracked the USS while 19.17, 19.39, and 28.14 tracked the FS. Data from radar 28.14 was found to exhibit anomalous behavior and was not included the reconstruction.

Table 4: Eastern Range Radar Specifications

Radar	Type	Latitude (deg N)	Longitude (deg E)	Geodetic Altitude (m)	Azimuth Error (mrad)	Elevation Error (mrad)	Range Error (ft)
19.17	MCBR	28.62593911	-80.68279958	-19.57	0.90	0.90	60
19.39	MPS-39	28.47857681	-80.67478864	-12.3	0.90	0.90	60
19.14	FPQ-14	28.4247112	-80.6643877	-17.35	0.20	0.40	60
28.14	FPQ-14	26.9830174	-80.1081835	-7.61	0.20	0.40	60

METEOROLOGICAL SENSORS

Meteorological data was available from Automated Meteorological Profiling System (AMPS) low resolution flight element (LRFE) and high resolution flight element (HRFE) weather balloon measurements acquired throughout the day of launch. The weather balloon data was used to support day of launch flight load assessments for go/no-go decisions as well as for trajectory reconstruction purposes to provide estimates of the freestream atmospheric conditions. Table 5 summarizes the balloon measurements and their sensor uncertainties. Note that the uncertainties only include the actual measurement uncertainty and do not include temporal and spatial uncertainties due to the balloon being located at a different point and a different time than the Ares I-X vehicle at a given altitude. The balloons provided atmospheric properties up to a maximum altitude of 100 kft. Marshall Space Flight Center's (MSFC) Natural Environments Group created an Ares I-X meteorological profile, referred to as the Ares I-X MET, up to 400 kft using data from the HRFE balloon released at L+0:05 minutes (1535 Z), the LRFE balloon released at L-0:55 minutes (1435 Z) and a mean October atmosphere defined by the Kennedy Space Center (KSC) 2006 Range Reference Atmosphere (RRA) and the Global Reference Atmosphere Model 2007 (GRAM2007), version 2. The MET was constructed from those data sources as follows: HRFE data was used from ground level to 50 kft. The HRFE data was blended into the LRFE data from 50 kft to 51 kft and LRFE data used up to 101 kft. The LRFE data was blended into the KSC 2006 RRA mean October atmosphere from 101 kft to 103 kft and the KSC 2006 RRA mean October atmosphere used up to 229 kft. The KSC 2006 RRA mean October atmosphere was blended into the GRAM 2007 mean October atmosphere from 229 kft to 232 kft and the GRAM 2007 mean October atmosphere used up to 232 kft to 400 kft. The MET data sources are documented in the Ares I-X final meteorological profile transmittal letter provided in Reference 3.

Table 5: Weather Balloon Specifications

MSL Altitude (kft)	Altitude Resolution (ft)	Winds Data Source	Winds Error (m/s)	Temperature, Pressure, Density Data Source	T Error (deg C)	p Error (mbar)	ρ Error (g/m^3)
< 55	100	HRFE	1.0	LRFE	0.2	0.5	0.5
55-100	1000	LRFE	1.5	LRFE	0.2	0.5	0.5
100-200	3000	RRA	From GRAM 07	RRA	From GRAM 07		
> 200	3000	GRAM 07	From GRAM 07	GRAM 07	From GRAM 07		

TRAJECTORY ESTIMATION PROCESS

The BET was calculated using a statistical trajectory estimation program known as NewSTEP. This trajectory estimation program is a Matlab-based Iterative Extended Kalman Filter (IEKF) code that computes optimal 6-DOF trajectory estimates based on all available measurement data along with uncertainty estimates. This code is a generalization of the Statistical Trajectory Estimation Program (STEP)[4] developed by NASA/LaRC and used extensively in the 1960s-1980s on a wide variety of launch vehicle and entry vehicle flight projects. The NewSTEP code borrows heavily from the STEP formulation, but includes several

enhancements to the algorithms and implementation, such as the addition of the iterative Kalman filter capability and new measurement types. Also, NewSTEP is coded entirely in Matlab in order to make use of built-in capabilities such as numerical integration and matrix algebra routines.[5,6]

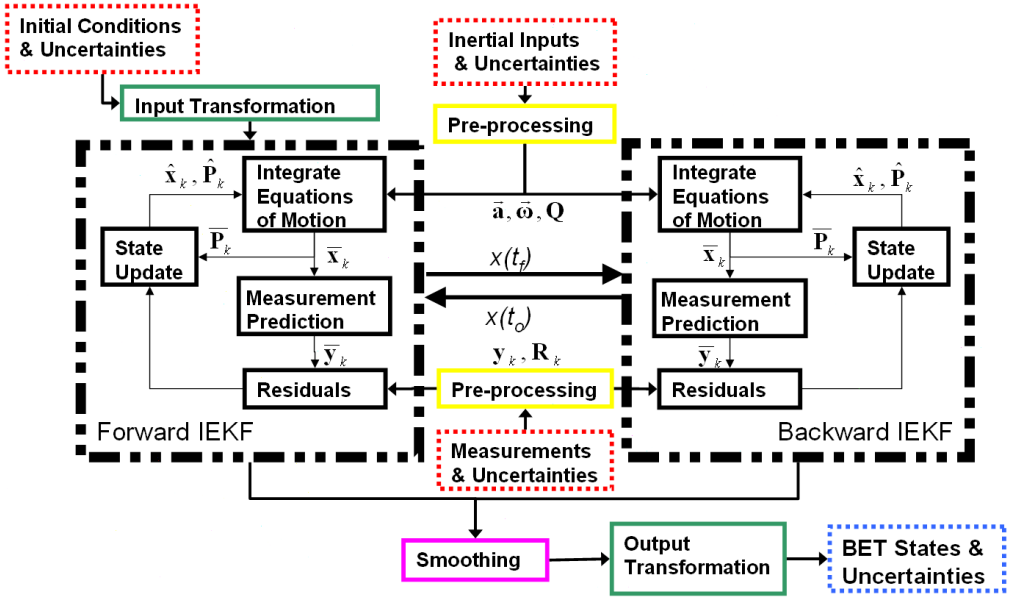

Figure 4: NewSTEP Flow Diagram

A flowchart illustrating the reconstruction data processing scheme implemented in NewSTEP is shown in Figure 4. The inputs to the reconstruction method consist of initial conditions, inertial measurement data in the form of linear accelerations and angular rates, and various observed quantities such as radar and air data measurements. Additionally, uncertainties on all these input data sources must be provided for the proper weighting to be assigned to the data in the filtering algorithm. It is important that the input uncertainties be realistic in order to avoid improper weighting: measurement data with uncertainties set erroneously low can introduce non-physical dynamics because the filter will essentially track the noise. These inputs are shown with the dashed red boxes in Figure 4. Pre-processing is conducted to perform any coordinate transformations that maybe necessary, and to improve data quality by reducing noise, eliminating systematic errors, and editing potentially bad data that sometimes can arise. The pre-processing and the input transformations are shown with the yellow and green boxes in Figure 4, respectively.

The core data processing algorithm consists of a forward and backward IEKF that together, when merged using the Fraser-Potter smoothing algorithm,[7] form optimal state estimates based on all available data. The forward and backward filter algorithms are shown in the black boxes in Figure 4. The Kalman filter algorithm is reviewed in more detail in the next section, but at a high level it is a predictor corrector algorithm in which state predictions are computed from numerical integration of the rigid body equations of motion, and corrections to the estimate are computed from a weighted least-squares fit of state to the observed data. The forward filter processes the data in this manner starting from the initial time, and propagating through all the observed data. Since the end point of the forward pass has benefited from all available measurement data, but the earlier points in the trajectory have benefited from data recorded only up to that time, a backward pass is implemented that propagates the state estimate back to the initial time point. These two passes are fused using the Fraser-Potter smoothing algorithm, so that each data point in the BET is estimated from all available data. The smoothing step is shown in the purple box in Figure 4.

Lastly, output transformations are conducted to generate estimates of quantities of interest, such as Mach number and dynamic pressure, which are not internal state variables estimated in the Kalman filter. These transformations include uncertainty transformations that map the internal state uncertainties into output uncertainties. The end result of this process is the BET, shown in the blue dashed box, which includes vehicle trajectory estimates along with uncertainties.

KALMAN FILTER ALGORITHM

The Kalman filter is a recursive weighted least-squares estimation procedure that optimally blends sensor data and mathematical models to produce minimum variance estimates of the system state. Let the system dynamics be represented by a mixed continuous-discrete nonlinear model of the form

$$\dot{\boldsymbol{x}} = \boldsymbol{f}(\boldsymbol{x}, \boldsymbol{u}, \boldsymbol{\eta}, t) \tag{1}$$

$$\boldsymbol{y} = \boldsymbol{g}(\boldsymbol{x}, \boldsymbol{u}, \boldsymbol{\xi}, t) \tag{2}$$

where $\boldsymbol{x}$ is the filter state with continuous dynamics, $\boldsymbol{u}$ is a deterministic input, $\boldsymbol{\eta}$ is a stochastic input to the equations of motion (process noise), $\boldsymbol{y}$ is the measurement that is available at discrete time intervals, and $\boldsymbol{\xi}$ is the measurement noise.

Let the quantities $\hat{\boldsymbol{x}}_{k-1}$ and $\hat{\boldsymbol{P}}_{k-1}$ be the state estimate and state estimate error covariance matrix at time t_{k-1}, respectively, and let $\bar{\boldsymbol{x}}_k$ and $\bar{\boldsymbol{P}}_k$ be the predicted state and covariance at time t_k, computed from numerical integration of the continuous process dynamics and the linear covariance propagation equation[8]

$$\dot{\boldsymbol{P}} = \boldsymbol{A}(t)\boldsymbol{P}(t) + \boldsymbol{P}(t)\boldsymbol{A}(t)^T + \boldsymbol{B}(t)\boldsymbol{Q}(t)\boldsymbol{B}(t)^T \tag{3}$$

where $\boldsymbol{A}(t)$ is the linearization of the system dynamics with respect to the state, $\boldsymbol{B}(t)$ is the linearization of the system dynamics with respect to the process noise inputs, and $\boldsymbol{Q}(t)$ is the process noise spectral density. Then, the measurement $\boldsymbol{y}_k$ at time t_k is processed according to[8]

$$\hat{\boldsymbol{x}}_{k,i+1} = \bar{\boldsymbol{x}}_k + \boldsymbol{K}_{k,i}\left[\boldsymbol{y}_k - \boldsymbol{g}(\hat{\boldsymbol{x}}_{k,i}, \boldsymbol{u}_k, \boldsymbol{\xi}_k, t_k) - \boldsymbol{C}_{k,i} \cdot (\bar{\boldsymbol{x}}_k - \hat{\boldsymbol{x}}_{k,i})\right] \tag{4}$$

where i denotes the iteration index and $\boldsymbol{C}$ is the linearization of the measurement model with respect to the state. The quantity $\boldsymbol{K}_{k,i}$ is the Kalman gain matrix, given by[8]

$$\boldsymbol{K}_{k,i} = \bar{\boldsymbol{P}}_k \boldsymbol{C}_{k,i}^T \left[\boldsymbol{C}_{k,i} \bar{\boldsymbol{P}}_k \boldsymbol{C}_{k,i}^T + \boldsymbol{D}_{k,i} \boldsymbol{R}_k \boldsymbol{D}_{k,i}^T\right] \tag{5}$$

where $\boldsymbol{R}_k$ is the measurement noise covariance matrix and $\boldsymbol{D}$ is the linearization of the measurement model with respect to the measurement noise.

The filtering equations listed above are iterated until convergence (or until reaching a prescribed iteration limit), leading to the state estimate that follows from the nonlinear measurement update. The covariance of the state estimate is computed from

$$\hat{\boldsymbol{P}}_k = \left[\boldsymbol{I} - \boldsymbol{K}_k \boldsymbol{C}_k\right] \bar{\boldsymbol{P}}_k \tag{6}$$

where $\boldsymbol{I}$ is the identity matrix of appropriate dimension.

After processing the IEKF forward and backward through all the available measurement data, the estimates are combined using the Fraser-Potter smoothing algorithm, given by[7]

$$\hat{\boldsymbol{P}}_k = \left[\hat{\boldsymbol{P}}_{f_k}^{-1} + \bar{\boldsymbol{P}}_{b_k}^{-1}\right]^{-1} \tag{7}$$

$$\hat{\boldsymbol{x}}_k = \hat{\boldsymbol{P}}_k \left[\hat{\boldsymbol{P}}_{f_k}^{-1} \hat{\boldsymbol{x}}_{f_k} + \bar{\boldsymbol{P}}_{f_k}^{-1} \bar{\boldsymbol{x}}_{b_k}\right] \tag{8}$$

where $\hat{\boldsymbol{x}}_{f_k}$ and $\hat{\boldsymbol{P}}_{f_k}$ are the forward filtered state and covariance estimates, $\bar{\boldsymbol{x}}_{b_k}$ and $\bar{\boldsymbol{P}}_{b_k}$ are the backward predicted state and covariance estimates, and $\hat{\boldsymbol{x}}_k$ and $\hat{\boldsymbol{P}}_k$ are the smoothed state and covariance estimates.

Note that the Kalman filter algorithm essentially assumes that the distributions of the uncertain inputs are Gaussian, characterized by their mean and covariance. In the Gaussian case, the Kalman filter is the maximum-likelihood and estimator. In the non-Gaussian case, no other linear estimator exhibits a lower variance than the Kalman filter. In this sense the Kalman filter is the best linear estimator, regardless of the actual noise distributions. Further information on assumptions inherent to this approach can be found in Reference 8.

COORDINATE SYSTEMS

Several coordinate systems must be defined before the filter state variables, which are based on Newtonian mechanics, are discussed. First, the vehicle body frame is illustrated in Figure 5. This frame has its origin at the vehicle center of mass, x-axis oriented forward, z-axis oriented along the "heads-down" direction, and y-axis defined such that the system is right handed.

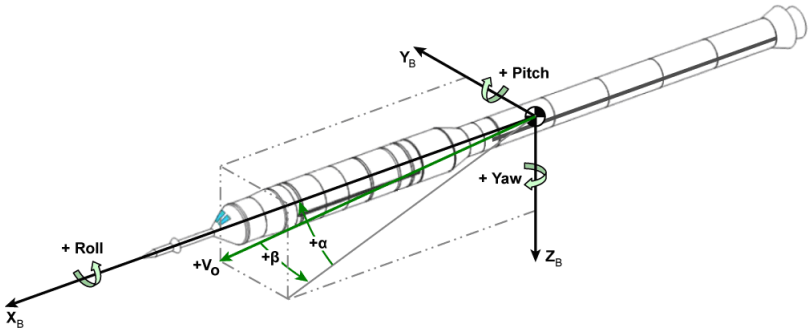

Figure 5: Body Axis Coordinate System

Next, the Earth-Centered Earth-Fixed (ECEF) and Geocentric (GC) frames are shown in Figure 6(a). The ECEF frame has its origin at the center of the Earth, the x-axis is fixed to the prime meridian, the z-axis is normal to the equator toward the north, and the y-axis is such that the system is right handed. The GC frame has its origin at the vehicle center of mass, with z-axis oriented toward the center of the planet, x-axis is normal to the radius vector in the northerly direction, and y-axis is to the East. The Geodetic (GD) frame is defined similarly to the GC frame but has its z-axis perpendicular to the reference ellipse and x-axis tangent to the reference ellipse in the north direction. The y-axis of the GD frame is the same as that of the GC frame.

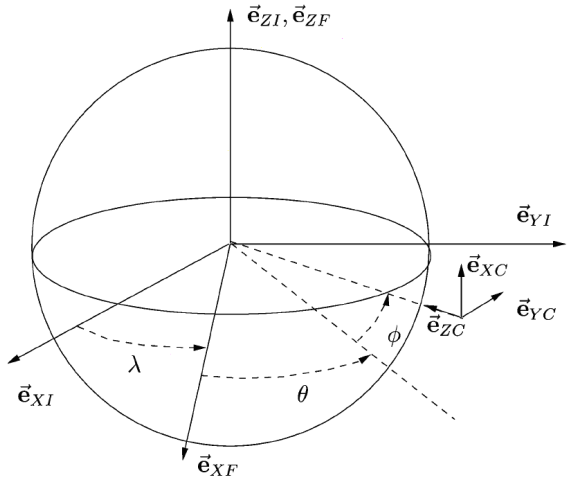

(a) ECEF and GC Coordinate Systems

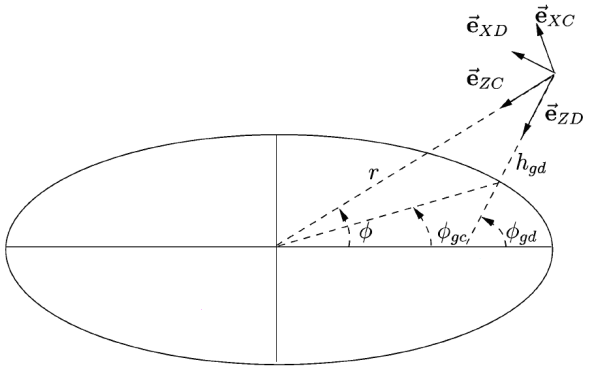

(b) Declination, Geocentric Latitude, and Geodetic Latitude

Figure 6: Coordinate Systems

EQUATIONS OF MOTION

The filter state variables used in this formulation are

$$\boldsymbol{x} = \begin{bmatrix} r & \theta & \phi & u & v & w & e_0 & e_1 & e_2 & e_3 & u_w & v_w & w_w & p & \rho \end{bmatrix}^T \tag{9}$$

where r is the radius of the vehicle from the center of the planet, θ is the longitude, ϕ is the declination, u, v, w are the inertial velocity components in the GC frame, e_i are the Euler parameters describing the attitude of the vehicle with respect to the GD frame, u_w, v_w and w_w are the wind components in the GD frame, and p and ρ are the freestream pressure and density, respectively.

The state dynamics are modeled with the nonlinear system of differential equations given by[5]

$$\dot{r} = -w \tag{10}$$

$$\dot{\phi} = \frac{u}{r} \tag{11}$$

$$\dot{\theta} = \frac{v}{r\cos\phi} - \Omega \tag{12}$$

$$\begin{Bmatrix} \dot{u} \\ \dot{v} \\ \dot{w} \end{Bmatrix} = \boldsymbol{G}^T \begin{Bmatrix} a_x + \eta_{a_x} \\ a_y + \eta_{a_y} \\ a_z + \eta_{a_z} \end{Bmatrix} + \begin{Bmatrix} \left(uw - v^2\tan\phi\right)/r - \left(3\mu J_2/2r^4\right)\sin\left(2\phi\right) \\ \left(uv\tan\phi + vw\right)/r \\ -\left(u^2+v^2\right)/r + \mu/r^2 - \left(3\mu J_2/2r^4\right)\left(2 - 3\cos^2\phi\right) \end{Bmatrix} \tag{13}$$

$$\begin{Bmatrix} \dot{e}_0 \\ \dot{e}_1 \\ \dot{e}_2 \\ \dot{e}_3 \end{Bmatrix} = \frac{1}{2}\begin{bmatrix} -e_1 & -e_2 & -e_3 \\ e_0 & -e_3 & e_2 \\ e_3 & e_0 & -e_1 \\ -e_2 & e_1 & e_0 \end{bmatrix} \left(\begin{Bmatrix} \omega_x + \eta_{\omega_x} \\ \omega_y + \eta_{\omega_y} \\ \omega_z + \eta_{\omega_z} \end{Bmatrix} - \frac{1}{r}\boldsymbol{G}\begin{Bmatrix} v \\ -u \\ -v\tan\phi \end{Bmatrix} \right) \tag{14}$$

$$\dot{p} = \frac{\mu\rho w}{r^2} + \eta_p \tag{15}$$

$$\dot{\rho} = \frac{\mu\rho^2 w}{r^2 p} + \eta_\rho \tag{16}$$

$$\dot{u}_w = \eta_{u_w} \tag{17}$$

$$\dot{v}_w = \eta_{v_w} \tag{18}$$

$$\dot{w}_w = \eta_{w_w} \tag{19}$$

where μ is the planetary gravitational parameter, J_2 is the planetary oblateness coefficient, Ω is the angular rate of the planet. The matrix $\boldsymbol{G}$ is the transformation from the GD frame to the body frame, given by $\boldsymbol{G} = \boldsymbol{G}_d\boldsymbol{G}_\phi$, where

$$\boldsymbol{G}_d = \begin{bmatrix} e_0^2 + e_1^2 - e_2^2 - e_3^2 & 2\left(e_1e_2 + e_0e_3\right) & 2\left(e_1e_3 - e_0e_2\right) \\ 2\left(e_1e_2 - e_0e_3\right) & e_0^2 - e_1^2 + e_2^2 - e_3^2 & 2\left(e_0e_1 + e_2e_3\right) \\ 2\left(e_1e_3 + e_0e_2\right) & 2\left(e_2e_3 - e_0e_1\right) & e_0^2 - e_1^2 - e_2^2 + e_3^2 \end{bmatrix} \tag{20}$$

$$\boldsymbol{G}_\phi = \begin{bmatrix} \cos\left(\phi - \phi_{gd}\right) & 0 & \sin\left(\phi - \phi_{gd}\right) \\ 0 & 1 & 0 \\ -\sin\left(\phi - \phi_{gd}\right) & 0 & \cos\left(\phi - \phi_{gd}\right) \end{bmatrix} \tag{21}$$

The quantities ω_x, ω_y and ω_z are the body-axis sensed angular rates, and a_x, a_y and a_z are body center of mass accelerations, which are computed from the IMU sensed accelerations and rates along with the associated lever arm correction. Additive process noise terms (η) are included on the acceleration and angular rate measurements to account for sensor errors. Process noise terms are also included on the atmospheric winds, pressure, and density to account for model uncertainties.

EQUATIONS OF MEASUREMENT

The Kalman filter requires a mathematical model for the measurements, written as a function of the state variables, to form residuals for the filter state update step. This section describes these measurement equations.

Inertial Measurement Unit

The NewSTEP filter has the ability to solve for systematic errors in the inertial acceleration and rate measurements, specifically bias, scale factor, and misalignment. Systematic errors in the inertial measurements for this particular vehicle were assumed to be smaller than the uncertainties introduced by the low frequency smoothing of the structural noise and were ignored.

Tracking Radar

The tracking radar measurements can be written as a function of the vehicle state by means of the transformations

$$R = \sqrt{x^2 + y^2 + z^2} \tag{22}$$

$$\sin\nu = \frac{y}{\sqrt{x^2 + y^2}} \tag{23}$$

$$\cos\nu = \frac{x}{\sqrt{x^2 + y^2}} \tag{24}$$

$$\sin\kappa = -\frac{z}{R} \tag{25}$$

where R, ν, and κ are the range, azimuth, and elevation from the tracking station to the vehicle, and x, y, and z are the components of the position of the tracking beacon relative to the station, represented in a geodetic frame location to the ground station, given by

$$\left\{ \begin{array}{c} x \\ y \\ z \end{array} \right\} = \boldsymbol{G}_s \left\{ \begin{array}{c} r\cos\phi\cos\theta - r_s\cos\phi_s\cos\theta_s \\ r\cos\phi\sin\theta - r_s\cos\phi_s\sin\theta_s \\ r\sin\phi - r_s\sin\phi_s \end{array} \right\} \tag{26}$$

where r, ϕ, and θ are the radius, declination, and longitude of the beacon with respect to the center of the Earth, and r_s, ϕ_s, and θ_s are the same quantities for the radar tracking station. The matrix $\boldsymbol{G}_s$ is the transformation between Earth Centered Earth Fixed (ECEF) coordinates and the local geodetic frame of the ground station, given by

$$\boldsymbol{G}_s = \left[\begin{array}{ccc} -\sin\phi_{gd_s} & 0 & \cos\phi_{gd_s} \\ 0 & 1 & 0 \\ -\cos\phi_{gd_s} & 0 & -\sin\phi_{gd_s} \end{array} \right] \cdot \left[\begin{array}{ccc} \cos\theta_s & \sin\theta_s & 0 \\ -\sin\theta_s & \cos\theta_s & 0 \\ 0 & 0 & 1 \end{array} \right] \tag{27}$$

where ϕ_{gd_s} is the geodetic latitude of the tracking station.

Additive bias terms are included on the range, azimuth, and elevation measurements in order to account for systematic errors in the radar data, which are treated as "solve-for" parameters in the filter.

Air Data Vanes

The air data vanes provide measurement of the local angle of attack and sideslip. After applying correction factors for upwash effects, these measurements are related to the internal filter state by the relations

$$\boldsymbol{v}_b = \boldsymbol{G}_d \left(\boldsymbol{G}_\phi \left\{ \begin{array}{c} u \\ v - r\Omega\cos\phi \\ w \end{array} \right\} - \left\{ \begin{array}{c} u_w \\ v_w \\ w_w \end{array} \right\} \right) + \left\{ \begin{array}{c} \omega_y z_v - \omega_z y_v \\ \omega_z x_v - \omega_x z_v \\ \omega_x y_v - \omega_y x_v \end{array} \right\} \tag{28}$$

$$\alpha_v = \arctan 2\left[\boldsymbol{v}_b(3), \boldsymbol{v}_b(1)\right] \tag{29}$$

$$\beta_v = \arctan 2\left[\boldsymbol{v}_b(2), \sqrt{\boldsymbol{v}_b(1)^2 + \boldsymbol{v}_b(2)^2}\right] \tag{30}$$

where α_v and β_v are the vane measurements and x_v, y_v and z_v are the position components of the vane with respect to the vehicle center of mass. Note that the velocity due to rotation with lever arm is accounted for in these transformations.

OUTPUT TRANSFORMATIONS

Auxiliary calculations are performed in order to transform the internal filter state into desired output quantities. For example, the angle of attack is not an internal filter state but it is a desired output from the trajectory reconstruction process. A mapping is utilized to transform the internal state variable uncertainties in the form of the state covariance matrix into the output variables, so that uncertainty bounds on these output parameters can be provided. This section outlines the transformations performed in order to compute these output quantities.

Planet-Relative Outputs

Planet-relative outputs such as geodetic altitude, h_{gd}, and latitude, ϕ_{gd}, illustrated in Figure 6(b), are calculated from the relations[9]

$$\tan\phi_{gd} = \tan\phi + \frac{e_\oplus^2 \sin\phi_{gd}}{r\cos\phi\sqrt{1-e_\oplus^2\sin^2\phi_{gd}}} \tag{31}$$

$$h_{gd} = \frac{r\cos\phi}{\cos\phi_{gd}} - \frac{R_\oplus}{\sqrt{1-e_\oplus^2\sin^2\phi_{gd}}} \tag{32}$$

where $e_\oplus$ and $R_\oplus$ are is the eccentricity and semimajor axis of the Earth's reference ellipsoid. Equation (31) is solved using Sofair's method.[10]

The mean sea level (MSL) altitude is calculated from the 360 degree and order EGM-96 geoid model, which provides the geoid offset as a function of latitude and longitude. The geoid offset is then subtracted from the geodetic altitude to give the MSL altitude.

The North-East-Down (NED) planet-relative velocity and the flight path angle and velocity azimuth angle are calculated from

$$\boldsymbol{v}_{ned} = \left\{ \begin{array}{c} v_n \\ v_e \\ v_d \end{array} \right\} = \boldsymbol{G}_\phi \left\{ \begin{array}{c} u \\ v - r\Omega\cos\phi \\ w \end{array} \right\} \tag{33}$$

$$\gamma = \arctan 2\left(-\frac{v_d}{\sqrt{\boldsymbol{v}_{ned}\cdot\boldsymbol{v}_{ned}}}, \frac{v_n^2+v_e^2}{\sqrt{\boldsymbol{v}_{ned}\cdot\boldsymbol{v}_{ned}}} \right) \tag{34}$$

$$\chi = \arctan 2\left(\frac{v_n}{\sqrt{v_n^2+v_e^2}}, \frac{v_e}{\sqrt{v_n^2+v_e^2}} \right) \tag{35}$$

Atmospheric-Relative Outputs

The atmospheric angle of attack and sideslip are calculated in a similar fashion to that of the air data vane measurement equations listed above, but here the output transformations involve the angle of attack and sideslip of the vehicle mass center rather than that of the vane. The total angle of attack (α_T) and aerodynamic roll angle (Φ_a) are also calculated as outputs. The transformations are

$$\boldsymbol{v}_b = \boldsymbol{G}_d \left(\boldsymbol{G}_\phi \left\{ \begin{array}{c} u \\ v - r\Omega\cos\phi \\ w \end{array} \right\} - \left\{ \begin{array}{c} u_w \\ v_w \\ w_w \end{array} \right\} \right) \tag{36}$$

$$\alpha = \arctan 2\left[\boldsymbol{v}_b(3), \boldsymbol{v}_b(1)\right] \tag{37}$$

$$\beta = \arctan 2\left[\boldsymbol{v}_b(2), \sqrt{\boldsymbol{v}_b(1)^2+\boldsymbol{v}_b(2)^2}\right] \tag{38}$$

$$\alpha_T = \arccos\left(\cos\alpha\cos\beta\right) \tag{39}$$

$$\Phi_a = \arctan 2\left(\sin\beta, \sin\alpha\cos\beta\right) \tag{40}$$

The Mach number, dynamic pressure, and Reynolds number (per foot) are calculated according to the relations

$$M = \sqrt{\frac{\rho\left(\boldsymbol{v}_b\cdot\boldsymbol{v}_b\right)}{\gamma_h p}} \tag{41}$$

$$q = \frac{1}{2}\rho\left(\boldsymbol{v}_b\cdot\boldsymbol{v}_b\right) \tag{42}$$

$$R_e = \frac{\rho\sqrt{\boldsymbol{v}_b\cdot\boldsymbol{v}_b}}{\mu_v} \tag{43}$$

where γ_h is the atmospheric ratio of specific heats. Note that the Reynolds number calculation involves the dynamic viscosity, μ_v, which is computed according to the Sutherland relations given in Ref. 11.

Earth-Centered Earth-Fixed Outputs

The Earth-Centered Earth-Fixed (ECEF) outputs are computed from the internal filter state variables from the transformations

$$x_F = r\cos\phi\cos\theta \tag{44}$$

$$y_F = r\cos\phi\sin\theta \tag{45}$$

$$z_F = r\sin\phi \tag{46}$$

$$\begin{Bmatrix} \dot{x}_F \\ \dot{y}_F \\ \dot{z}_F \end{Bmatrix} = \begin{bmatrix} \cos\phi\cos\theta & -\sin\theta & -\sin\phi\cos\theta \\ \cos\phi\sin\theta & \cos\theta & -\sin\phi\sin\theta \\ \sin\phi & 0 & \cos\phi \end{bmatrix} \begin{Bmatrix} -w \\ v - r\Omega\cos\phi \\ u \end{Bmatrix} \tag{47}$$

The ECEF to body Euler parameters are extracted from the transformation matrix

$$\boldsymbol{G}_E = \boldsymbol{G}_d \cdot \begin{bmatrix} \cos(\phi_{gd} + \pi/2) & 0 & \sin(\phi_{gd} + \pi/2) \\ 0 & 1 & 0 \\ -\sin(\phi_{gd} + \pi/2) & 0 & \cos(\phi_{gd} + \pi/2) \end{bmatrix} \cdot \begin{bmatrix} \cos\theta & \sin\theta & 0 \\ -\sin\theta & \cos\theta & 0 \\ 0 & 0 & 1 \end{bmatrix} \tag{48}$$

Inertial (True of Date) Outputs

Vectors represented in the International Terrestrial Reference System (ITRS) are transformed to the inertial True of Date system consistent with the IAU 2000 resolutions as implemented by the International Earth Rotation and Reference Systems Service (IERS). The ITRS is defined as a rotating reference system, with its origin at the Earth's centroid, aligned with the conventional cartographic equator and prime meridian; it is equivalent to the Earth-Centered Earth-Fixed (ECEF) terminology used elsewhere in the text. The ITRS realizations are equivalent to the World Geodetic Survey of 1984 (WGS84) frame to within 10 cm. An intermediate inertial frame, the True of Date frame, is defined by the instantaneous equator and equinox of the launch epoch, 15:30:00.177 UTC on 28 Oct 2009. The transformation from ITRS to True of Date involves correction for polar motion (Xp = 241.059205 mas, Yp = 262.989745 mas) and the observed difference in civil and solar time of 173.506303 ms (UT1-UTC) as obtained from IERS Bulletin B262, Reference 12. The Greenwich Apparent Sidereal Time at the launch epoch is 269.6123486 degrees. Expressions to derive Greenwich Sidereal Time and the details of the transformation to the True of Date frame are available in IERS Conventions 2003 in Reference 13.

Uncertainty Transformation

The uncertainty of every derived quantity can be estimated by transforming the internal filter state covariance into the output coordinates. This mapping can be made by using the central difference transform, which provides second-order accuracy and does not require the use of any partial derivatives. The transformation is given in Ref. 14.

FLIGHT DATA PREPROCESSING AND UNCERTAINTY ANALYSIS

As discussed earlier in the BET process description, preprocessing must be performed on the flight data in order to improve data quality, adjust for latencies, and to transform the data into a format suitable for NewSTEP inputs. All telemetered data used in the development of the BET was taken from the Huntsville Operations Support Center (HOSC) Revision 14 database. This data was used to support BET development for the FTV ascent as well as the first stage descent. The development of the USS descent BET did not utilize any telemetered data and relied solely on range radar and the balloon-based MET profile.

Telemetry channels used for the reconstruction of the ascent and first stage entry are listed in Table 6. The Y and Z body accelerations from the FTINU were obtained from channels AKK239E and AKK240E, which were computed onboard to serve as inputs to the pitch/yaw control law's anti-drift algorithm. Since the X body acceleration was not computed onboard, it was calculated by multiplying channel CGK151C (IMS Z mount delta-V, where the Z mount axis corresponds to the -X body axis) by a factor of -50 to change the axis sign and to account for division by the accumulation interval of 20 ms.

Table 6: Telemetry Channels

Measurement	Telemetry Channel	Usage
FTINU Roll, Pitch, and Yaw Rates	CGK260C, CGK261C, CGK262C	FTV Ascent
FTINU X delta V	CGK151C	FTV Ascent
FTINU Y and Z (body) Accelerations	AKK239E and AKK240E	FTV Ascent
Forward RRGU Pitch Rates	BKK400E, BKK401E, BKK402E	FTV Ascent
Forward RRGU Yaw Rates	BKK403E, BKK404E, BKK405E	FTV Ascent
Aft RRGU Pitch Rates	BKK406E, BKK407E, BKK408E	FTV Ascent
Aft RRGU Yaw Rates	BKK409E, BKK410E, BKK411E	FTV Ascent
Alpha (Angle of Attack) Vane	OKD990H	FTV Ascent
Beta (Angle of Sideslip) Vane	OKD991H	FTV Ascent
SIGI Roll, Pitch, and Yaw Rates	AKD555B, AKD556B, AKD557B	FS Entry
SIGI X, Y, and Z Accelerations	AKD543A, AKD544A, AKD545A	FS Entry

INERTIAL MEASUREMENT UNIT DATA PREPROCESSING

The trajectory reconstruction plan for the FTV ascent was to combine FTINU, SIGI, and RRGU inertial acceleration and angular rate data to improve the estimate of the FTV rigid body acceleration and angular rates. The FTINU and SIGI accelerations and the FTINU, SIGI, and RRGU angular rates were to be blended into one composite set of inertial acceleration and angular rates referenced to the vehicle center of mass in the body frame. However, the SIGI data was not included in the blending process as originally intended since its accelerations exhibited significantly more noise than the FTINU, shown in Figure 7(a). The noise was thought to arise from the SRM motor acoustics exciting the SIGI which was mounted on the first stage avionics module (FSAM) in the FS. A power spectral density analysis of the signals revealed that the noise appeared to be broadband indicating that low-frequency noise was likely present. Such noise cannot be distinguished from the rigid-body dynamics and cannot be removed by smoothing. As a result, only the FTINU data was used for accelerations and only the FTINU and RRGU angular rates were combined during ascent. The FTINU and RRGU data ended at separation and the SIGI inertial data (acceleration and body angular rate) was used for reconstruction of the first stage descent trajectory.

Ascent IMU Data Preprocessing

During ascent, the FTINU and RRGU pitch and yaw rates were blended together to produce improved estimates of these parameters. The roll rate was based entirely on the FTINU. The pitch and yaw rates were blended according to the weighted averaging formula

$$\sigma_\omega^2 = \left(\sigma_{\omega_{FTINU}}^{-2} + \sigma_{\omega_{FRRGU}}^{-2} + k\sigma_{\omega_{ARRGU}}^{-2}\right)^{-1} \quad (49)$$

$$\omega = \sigma_\omega^2 \left(\sigma_{\omega_{FTINU}}^{-2}\omega_{FTINU} + \sigma_{\omega_{FRRGU}}^{-2}\omega_{FRRGU} + k\sigma_{\omega_{ARRGU}}^{-2}\omega_{ARRGU}\right) \quad (50)$$

where σ^2 denotes the variance of the signal.

The same formula was used for both pitch and yaw rate blending. The multiplier k on the ARRGU accounts for shock at liftoff due to the proximity of the ARRGU to the hold-down bolts on the SRM aft skirt. Due to the proximity of the ARRGU to the hold-down bolts, the ARRGU was exposed to a mechanical shock as the bolts were cut and the loads they were holding were released. The shock transient only affected the first half-second of the ARRGU data thus k is set to zero for first 0.5 sec and then increased linearly to unit magnitude at 1.0 sec. Note that this blending is performed after the RRGU rates have been center-selected and rotated into body axes. Additionally, a misalignment in the FRRGU was identified and corrected in the transformation to body axes. A summary of the alignment corrections utilized for the FRRGU for the BET are shown in Table 7. These alignment corrections describe the simultaneous rotation from the ideal (designed) FRRGU mounting to the estimated alignment of the actual FRRGU mounting in the flight vehicle.

After blending, the pitch and yaw rates were smoothed using an optimal Fourier filter to remove sensor noise, structural vibration, and to smooth the quantization effects, with 1 Hz cutoff frequency. Angular accelerations were computed by differentiation of a piecewise Hermite interpolating polynomial.

Table 7: FRRGU Alignment Corrections

Rotation	Value (deg)
Roll	0.7337
Pitch	-0.0738
Yaw	-0.2546

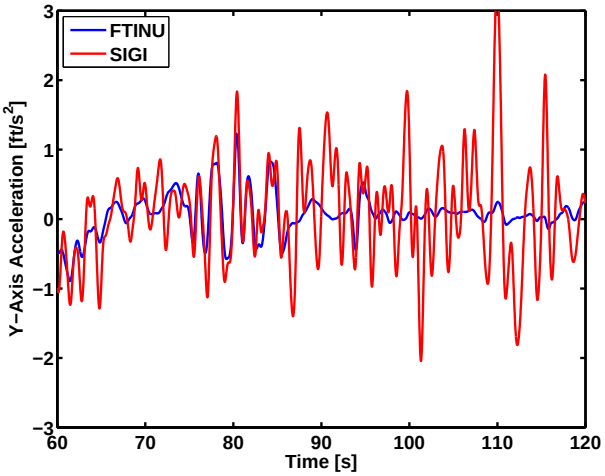

(a) Example of SIGI Noise

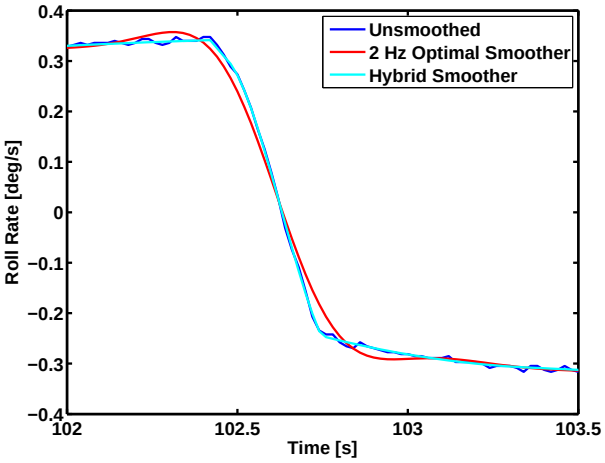

(b) Roll Rate Smoothing

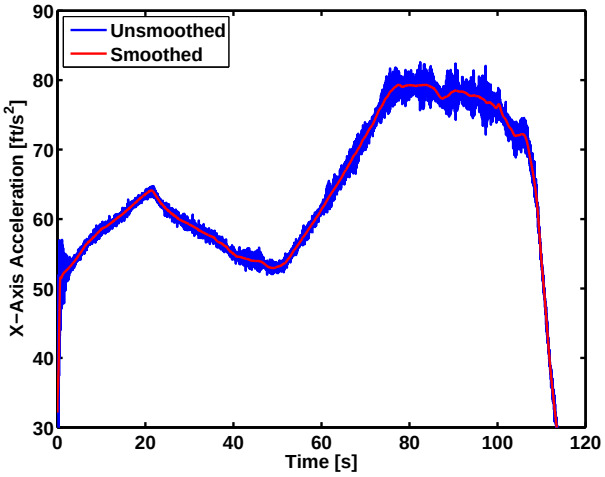

(c) Axial Acceleration Smoothing

Figure 7: IMU Preprocessing and Smoothing

The FTINU was the only usable data source for body roll rate since the SIGI had data quality problems and the RRGUs only measured pitch and yaw rates. The FTINU roll rate data exhibited large transients due to the RoCS thruster firings and required smoothing. Smoothing the FTINU roll rate during ascent was a trade-off between removing the vehicle structural response while maintaining the roll dynamics during the thruster firings. Even with the scheduled frequencies, it was not possible to smooth through the thruster firings without introducing smoothing artifacts (oscillations not present in the original data) prior to, during, and subsequent to the thruster firings. Instead, an ad hoc method, referred to as hybrid smoothing, was developed to smooth the ascent roll rate data. The input data was broken into time-based segments, with each segment being smoothed separately. The non-RoCS segments were smoothed using a 1 Hz optimal

Fourier smoother, while low-order polynomial curve fits were applied to segments during RoCS thruster firings. In some cases, short gaps between the segments were filled in with linear extrapolation from the adjoining segments to their point of intersection. Figure 7(b) shows a comparison of a 2 Hz optimal Fourier smoothing and the hybrid smoother in a region of RoCS firing.

After blending and smoothing of the angular rates, the FTINU accelerations were transformed to the vehicle center of mass and then smoothed to remove structural and measurement noise. The smoothing was performed using windows to capture the step input at motor ignition. Specifically, a 2 Hz optimal Fourier filter was used from time zero through 1.5 seconds. From 1.5 to 3.0 seconds, the filter frequency was ramped linearly from 2 Hz to 1 Hz. From 3.0 seconds through stage separation a 1 Hz filter was used. Figure 7(c) shows the unsmoothed and smoothed axial acceleration.

Descent IMU Data Preprocessing

The SIGI produced outputs at 50 Hz; however a timestamp was not associated with its data. The SIGI data were then over-sampled by the instrumentation system and output at a rate of approximately 80 Hz with an associated timestamp. That lead to duplication of some of the samples, which, along with the fact that no timestamp was produced for the original 50 Hz sampling, leads to a lack of a reliable time scale for the SIGI data. To work around this limitation, an artificial time scale with 20 ms intervals was constructed (starting at 15:30:00.177 UTC). The over sampled 80 Hz SIGI data were downloaded from the HOSC (version 014) one channel at a time, and for each point in the synthesized 50 Hz timescale, the HOSC data with the nearest timestamp was selected. Data points whose HOSC timestamp was more than 6.2 ms different from the synthesized SIGI 50 Hz timestamp were discarded as stale (i.e. the HOSC did not contain a sample for that channel within 6.2 ms of the selected time point). Points were automatically discarded if the values exceeded the high or low limit listed in Table 8, or varied from the preceding point by more than the maximum difference value listed in Table 8. Finally, all discarded points were filled in via linear interpolation using the valid points. Details of these limits, discarded points, and interpolations are shown in Table 8. Note that the total number of interpolations performed is equal to the sum of the number of stale frames, limit violations, and excess differences. In Table 8, note that the axes (X, Y, Z, Roll, Pitch, Yaw) refer to the SIGI mount axes and not vehicle body axes.

Table 8: SIGI Limits, Discarded Points, and Interpolations

Channel	Low Limit	High Limit	Max Diff.	Stale Frame	Out of Limits	Excess Diff.	Longest Gap
X Accel	-150 ft/s^2	200 ft/s^2	60 ft/s^2	1720	1	1	0.2 s
Y Accel	-200 ft/s^2	140 ft/s^2	60 ft/s^2	1720	1	2	0.2 s
X Accel	-170 ft/s^2	130 ft/s^2	120 ft/s^2	1724	4	1	0.2 s
Roll Rate	-25 deg/s	23 deg/s	2.5 deg/s	1717	3	1	0.2 s
Pitch Rate	-61 deg/s	33 deg/s	4.0 deg/s	1717	3	1	0.2 s
Yaw Rate	-45 deg/s	45 deg/s	4.0 deg/s	1722	4	2	0.2 s

Since the time of the original SIGI samples is not available, the re-constructed SIGI timescale was synchronized with other data to ensure that it was correct. The FTINU data was used for this purpose, and it was compared with the SIGI data during ascent to assess the comparative timing. The SIGI timescale was then adjusted by 20 ms increments (i.e. no interpolation of the data were necessary), which should result in a maximum of 10 ms error in the timescale. The SIGI rates (transformed to body axes) were compared with the FTINU rates and the SIGI timescale was adjusted to minimize the RMS of the residual (SIGI rate - FTINU rate). For all three rates (pitch, yaw, and roll), a one-frame advance (i.e. subtract 20 ms from the timescale) of the SIGI data made the best match with the FTINU. A similar exercise was attempted with the SIGI accelerometer data (with the FTINU accelerations transferred to the SIGI location for comparison), but the excessive noise present in the SIGI accelerometer channels precluded this approach. A visual comparison between the (transferred) FTINU accelerations and the SIGI accelerations showed that the same one frame advance appeared to give a reasonable match to the liftoff transient observed in the accelerometer channels, so the same one frame advance was applied to both the accelerometer and rate data from the SIGI.

The SIGI data were provided in SIGI mounting (mount) axes, and needed to be transformed to vehicle body axes for trajectory reconstruction. The nominal mounting was with the unit -Z axis parallel to the body +X axis, along with a 42-degree rotation (about the mount Z axis) pre-programmed into the SIGI as a boresight correction. The transform from mount to body would then consist of negating the Z axis (the mount axes are a left-hand system), followed by a 90 degree rotation about the Y axis. An equation error identification (similar to that performed on the forward RRGU) was performed on the SIGI gyros, resulting in an additional rotation of 7.557 degrees about the X axis to align the SIGI with the FTINU. This transformation was applied to both the rates and accelerations to produce body-axis SIGI outputs.

The SIGI signals, both rates and accelerations, were smoothed to reduce the structural response (and other noise) while preserving the rigid body dynamics. This was challenging due to the various transient events (stage separation, parachute releases, etc.) combined with significant noise content (especially in the accelerometer channels). Fourier smoothing was used, but the cutoff frequency was varied throughout the descent. Higher cutoff frequencies were used to preserve content during transient events, while lower cutoff frequencies were used during periods of high noise.

IMU Data Uncertainty Analysis

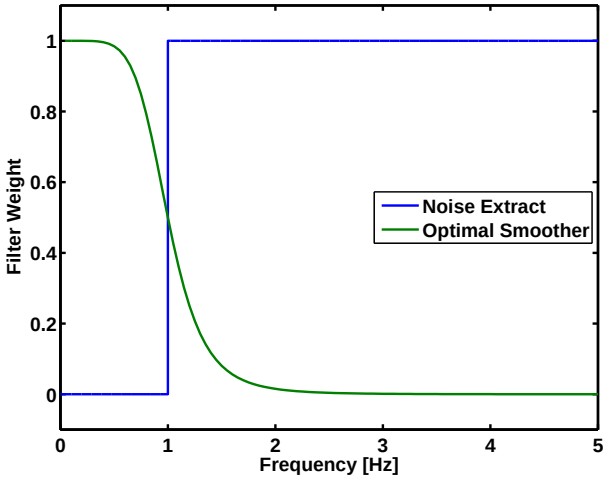

(a) Noise Extraction Filter

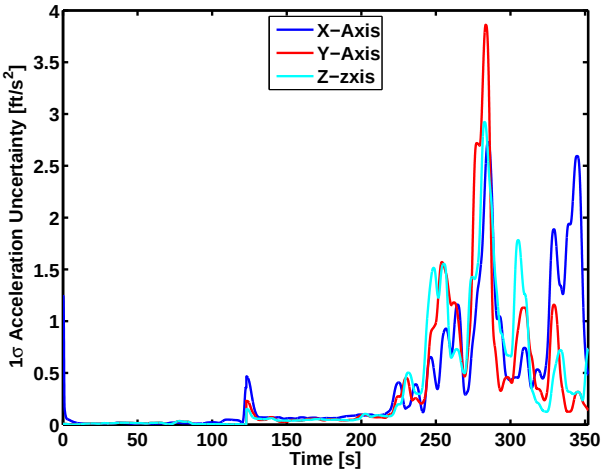

(b) Acceleration Uncertainty

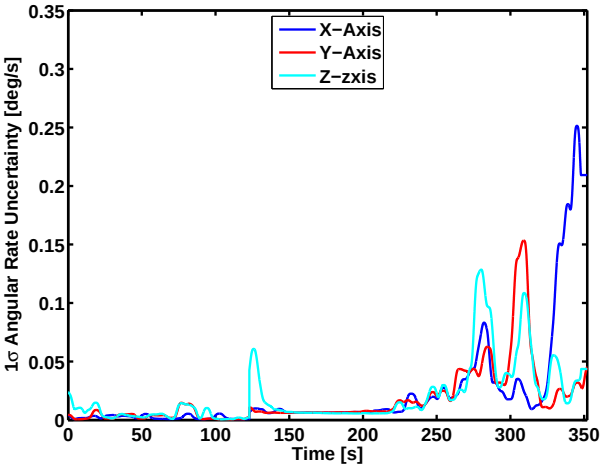

(c) Angular Rate Uncertainty

Figure 8: IMU Uncertainty

Uncertainties in the smoothed accelerations were estimated using a two step smoothing procedure.

First, noise components were isolated using a high-pass noise extraction filter with frequency cutoff of 1 Hz. The weights of this filter are shown in Figure 8(a). Next, the resulting noise components were passed through the optimal Fourier smoother to generate the residuals. The optimal Fourier smoother filter weights are also shown in Figure 8(a). The 3-σ process noise estimates were determined by fitting a bounding curve to these residuals using a 100 point sliding window. The uncertainty estimates were generated for the ascent trajectory using the STARS simulation, which includes known structural modes. The first-stage entry uncertainty estimates were constructed from the flight sensed accelerations and rates. The resulting uncertainties were root sum squared with the sensor accuracies and signal quantization intervals to produce the total IMU uncertainties used as the process noise spectral density in the Kalman filter. The resulting acceleration and rate uncertainties are shown in Figure 8(b) and (c), respectively.

RADAR DATA PREPROCESSING

Significant preprocessing was performed on the radar data to eliminate data that appeared to be physically invalid. All data from the 28.14 radar were removed from consideration due to erroneous tracking data. The 28.14 radar track showed an oscillation in the north velocity component which was not supported by other flight data. The oscillation could have been due to an unstable master frequency oscillator resonating with the intermediate frequency oscillator. This resonance produced a harmonic character in the range tracking data. Harmonic oscillations of this kind were physically unrealistic and therefore this data was neglected in the BET. The other tracks from 19.14, 19.17, and 19.39 were usable, although there were periods of dropouts and loss of beacon lock. Data during the time spans where dropouts or loss of beacon lock occurred were not used in the trajectory reconstruction. Additionally the smoothing performed by the radar operators introduced various artifacts such as ringing before and after dropout periods, which required further editing to remove. The time spans over which radar data was used is given in Table 9.

Table 9: Radar Time Spans

Radar	Time Spans (seconds from 15:30:0.177 Z)
19.14	24.74–88.74, 107.74–113.74
19.17	40.04–54.74, 93.04–116.94, 125.04–290.0
19.30	14.74–116.94, 125.04–134.75, 154.75–290.0

Uncertainties delivered with the radar data only accounted for the noise in the signal. The FTV position reported by the three radars differed by more than the uncertainty due to signal noise, which indicated the presence of systematic error and noise uncertainties much larger than those delivered with the radar data. As a result, the uncertainties delivered with the radar data were deemed to be unrealistically low. Realistic error uncertainties were accounted for by including the same uncertainties that are used for the Shuttle BET based on Reference 15, namely 10 meter noise uncertainty for the range measurement and 0.00015 radians for azimuth, and 0.0002 radians for elevation on all radar. Systematic errors in the radar data in the form of range, azimuth, and elevation biases were included in the Kalman filter state vector as solve-for parameters. These biases are modeled in the filter as unknown constants with initial 1-σ uncertainties based on Reference 15 of 12 meters for range, 0.0001 radians for azimuth, and 0.00015 radians for elevation. Figure 9 provides a comparison of the delivered versus adjusted uncertainties. The first column of plots shows the differences between the three radar tracks and a pure-inertial reconstruction based on direct numerical integration of the accelerations and angular rates alone, along with the delivered uncertainty bounds, transformed into an Up-South-East rectangular coordinate system centered on the launchpad. These plots indicate that the radar tracks are not self-consistent in the sense that the uncertainty bounds do not overlap over the majority of the trajectory. The second column of plots shows the same set of data but with the adjusted uncertainty bounds based on Reference 15. By adjusting the uncertainties, the tracks are consistent, providing realistic weighting of the data. For comparison, the post-flight corrected radar data based on solving for biases in the Kalman filter are shown in Figure 10. These plots illustrate that the filter is able to correct for systematic error in the radar tracks to further improve the trajectory estimate.

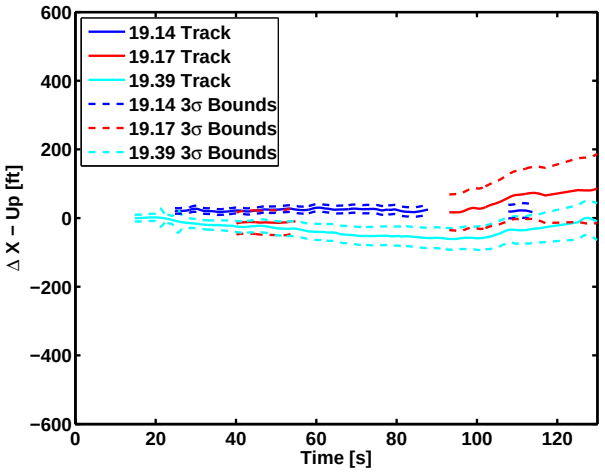

(a) Original Uncertainties: ΔX

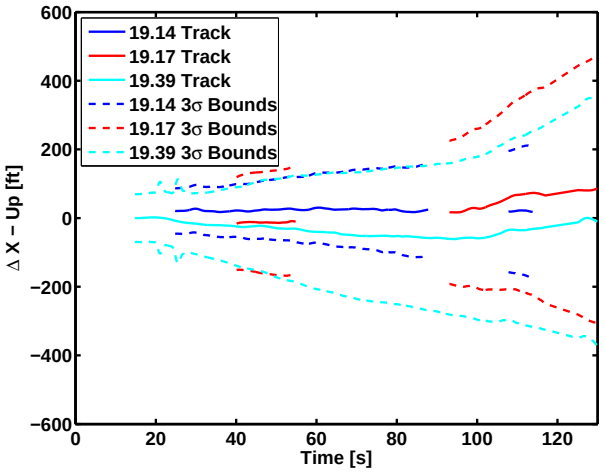

(b) Adjusted Uncertainties: ΔX

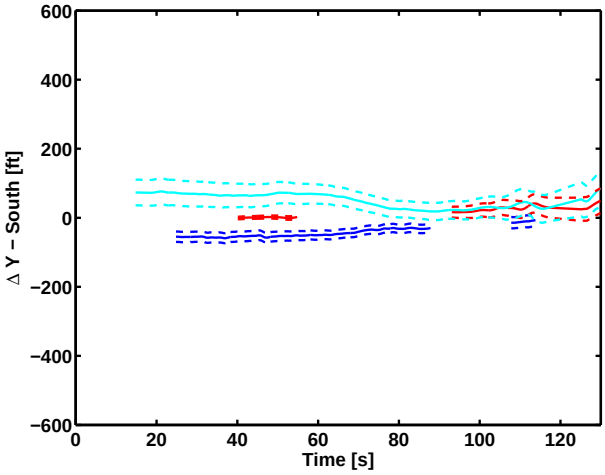

(c) Original Uncertainties: ΔY

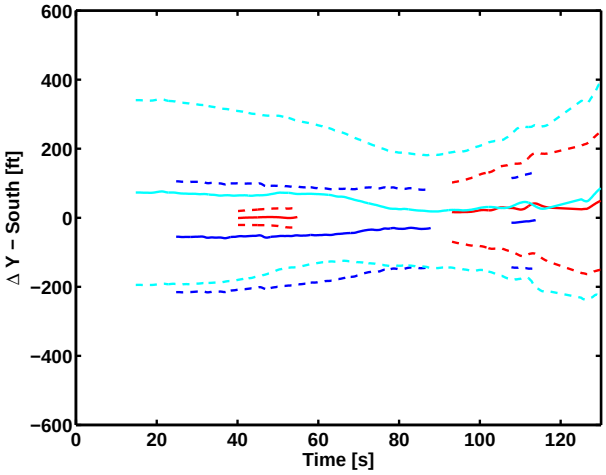

(d) Adjusted Uncertainties: ΔY

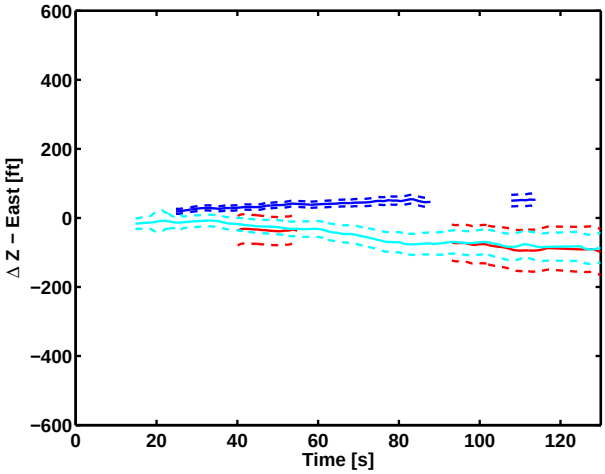

(e) Original Uncertainties: ΔZ

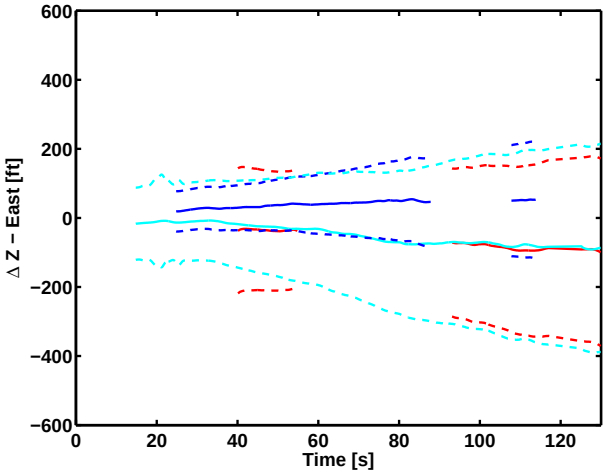

(f) Adjusted Uncertainties: ΔZ

Figure 9: Radar Uncertainties

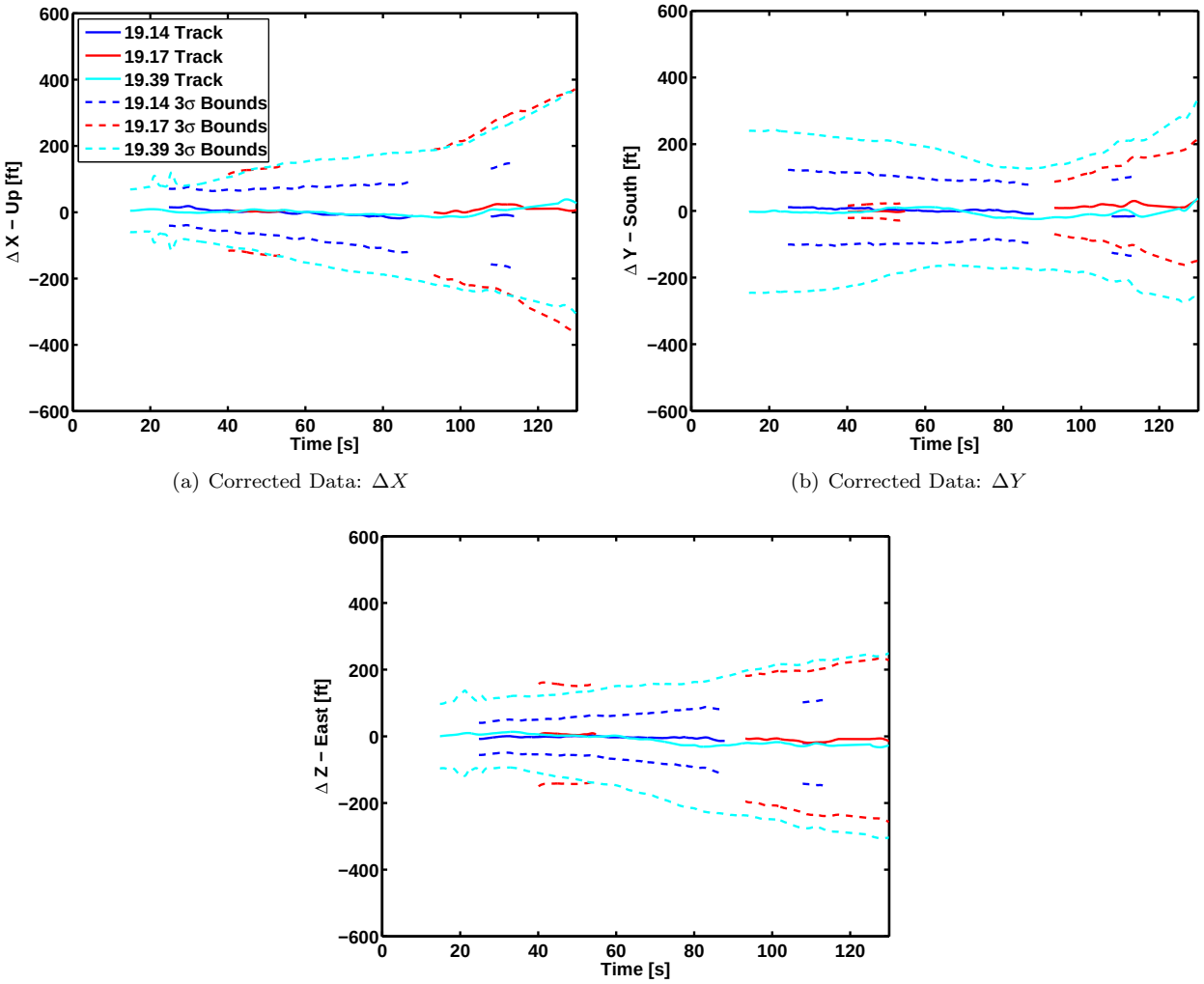

(a) Corrected Data: ΔX

(b) Corrected Data: ΔY

(c) Corrected Data: ΔZ

Figure 10: Corrected Radar Data

AIR DATA VANE PREPROCESSING

The vane data preprocessing consisted of creating a data set with a uniform 50 Hz frequency, applying a correction factor to the data to account for the vane's upwash effect on the air flow, and removing invalid data points. The vane data were telemetered by the instrumentation system at a rate of approximately 80 Hz. The intervals between timestamps were not precisely uniform, but rather varied slightly. The timescale was therefore replaced by a uniform timescale with an interval equal to the average interval (approximately 0.012288 sec of the original timescale). The vane data were then passed through a 20 Hz optimal Fourier smoother to provide anti-aliasing, and then the data were down-sampled (via cubic Hermite interpolation) to a uniform 50 Hz timescale, in order to match the 50 Hz time steps used in the trajectory reconstruction. CFD-based upwash correction factors were applied to the uniform 50 Hz data to account for localized flow conditions. The uncorrected and corrected vane data based on the upwash factors are shown in Figure 11. Lastly, data which did not appear to be valid were removed. In particular, data prior to 3.6 seconds after launch and data after 115 seconds were removed due to signs of hysteresis.

The vane uncertainties were made a function of time based on judgment that combines sensor accuracy, systematic error, and uncertainties in the upwash correction factors. In addition, elimination of vane data prior to 3.6 seconds required its uncertainty to be made large at 3.6 seconds to prevent the abrupt introduction of vane data as a redundant measurement from producing a step change in the FTV aerodynamic angles.

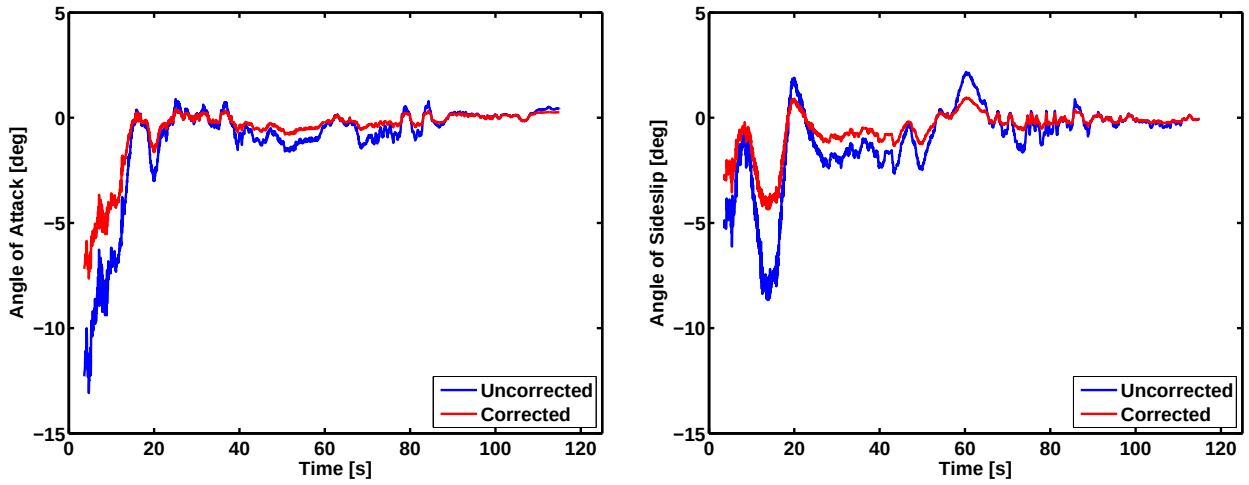

(a) Angle of Attack

(b) Angle of Sideslip

Figure 11: Air Data Vane Measurements

The vane 1-σ uncertainty was set to 100 degrees at 3.6 seconds and then linearly ramped down to 10 degrees at 4.6 seconds, and then ramped down again to 1 degree at 6.1 seconds. After 6.1 seconds, the uncertainty was held constant at 1 degree. The uncertainties were ramped down from 100 degrees to 1 degree in the manner described above in order to smooth the transition and avoid step changes in the atmospheric relative attitude and adjusted wind profiles.

ATMOSPHERIC DATA PREPROCESSING

The Ares I-X MET developed by MSFC's Natural Environments Group represented the best approximation of the atmospheric conditions flown through. MSFC's Natural Environments Group constructed the MET from balloon data up to 100 kft (the balloon's maximum altitude) and from mean October atmospheric properties defined by the 2006 KSC Range Reference Atmosphere and GRAM 2007 above 100 kft. The MET was a finished product not requiring preprocessing other than putting the data into the input format required by NewSTEP.

Uncertainty in the MET arose from two sources, sensor measurement uncertainty and uncertainty due to the temporal and spatial difference between the balloon ascent and the FTV trajectory. Measurement uncertainties were taken from the sensor specifications. A statistical estimate of the change in atmospheric thermal quantities and winds over time was not available from historical data. Temporal and spatial uncertainties were determined by MSFC's Natural Environments Group by examining changes in atmospheric thermal quantities and winds measured by six LRFE balloons released at 0800, 0900, 1000, 1100, 1200, and 1300 UTC. The change over the one hour interval between each set of balloon data was calculated as a function of altitude, and the RMS value of the five differences was used to approximate a combined temporal and spatial 1-σ uncertainty. For non-scalar quantities, the difference was calculated as a vector difference. The one hour differences included spatial uncertainty since the variation in winds resulted in the balloons ascending along different paths. The balloon data altitude uncertainty was 100 ft. Pressure and density were not measured quantities but were calculated using the ground reference pressure and temperature at altitude. Figure 12 shows the results of calculating RMS values as a function of altitude for one hour balloon differences. The 1-σ uncertainty input to the BET was the piecewise linear bounding functions that encapsulate the one hour balloon differences. Note that above 100 kft, the atmosphere uncertainties revert back to the KSC Range Reference and GRAM07 monthly mean uncertainties. Also, lacking vertical wind speed measurements it is assumed that the mean vertical wind component is zero with a 3-σ uncertainty of 10 ft/s.

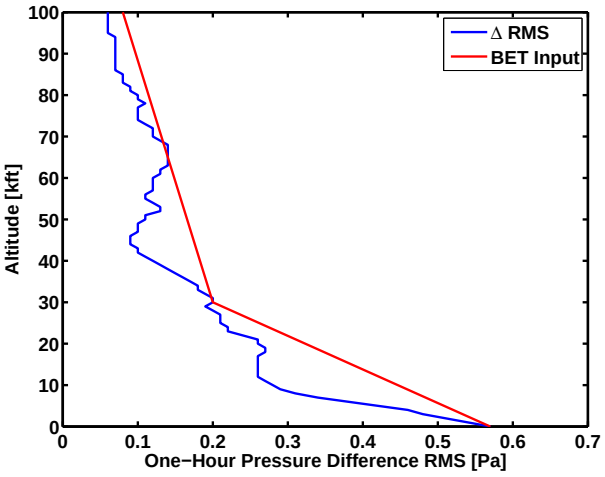

(a) Pressure Uncertainty

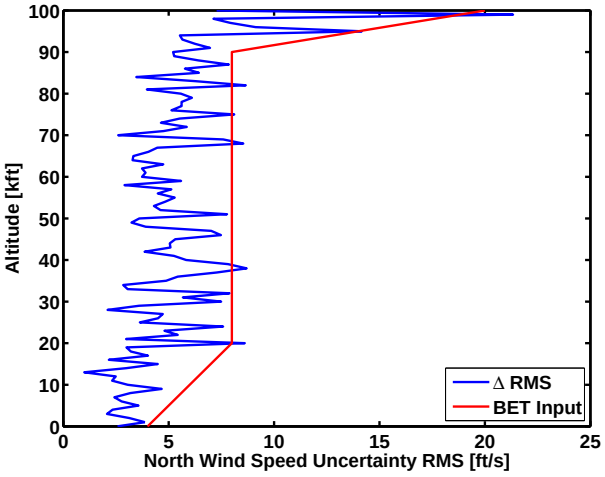

(b) North Wind Uncertainty

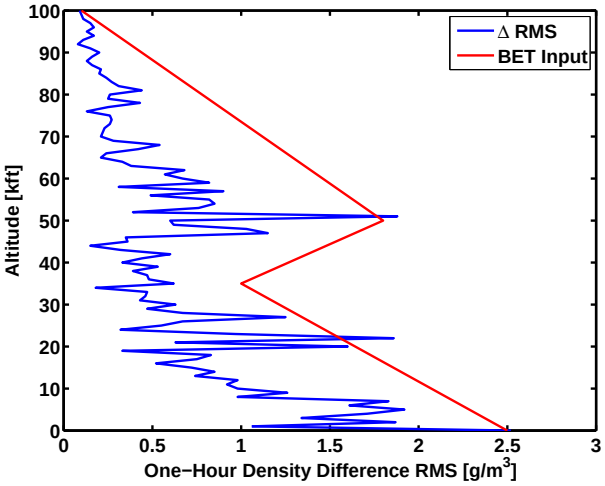

(c) Density Uncertainty

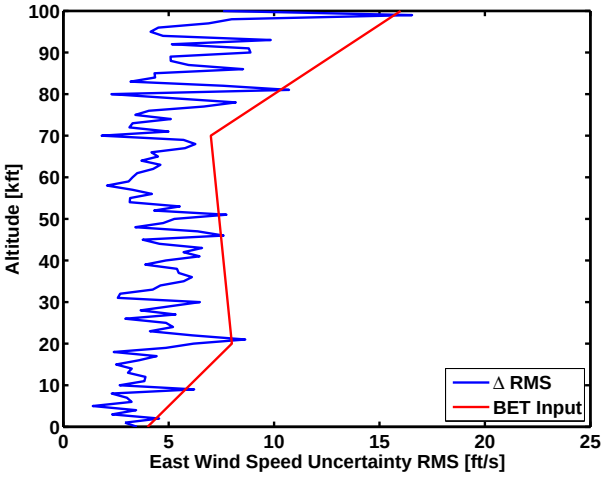

(d) East Wind Uncertainty

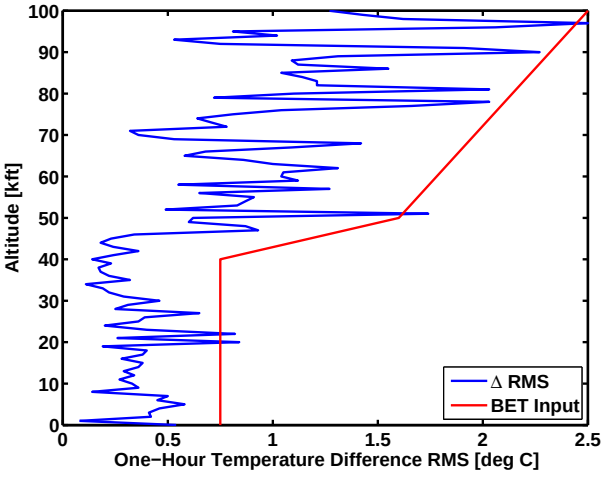

(e) Temperature Uncertainty

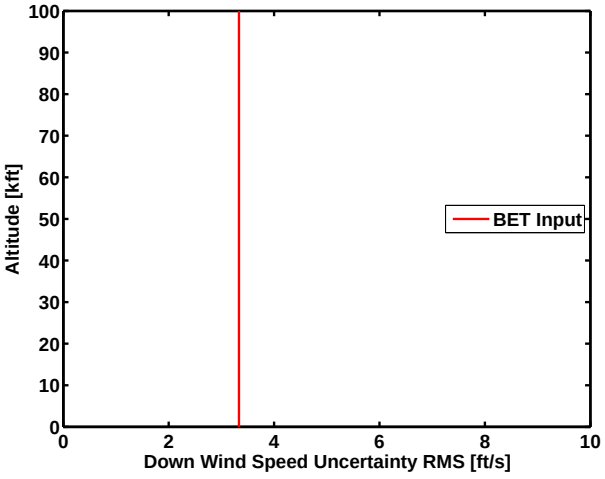

(f) East Wind Uncertainty

Figure 12: Atmospheric Uncertainties

BET RESULTS

In this section, the BET is compared to a Monte Carlo analysis using preflight models to show the flight values relative to pre-flight predicted bounds. The Monte-Carlo analysis was conducted for the October launch month using the Global Reference Atmospheric Model (GRAM) 2007, randomly dispersed October atmosphere and system parameters such as actuator, aerodynamics, and mass properties. A post-flight simulation was created by updating the October preflight simulation models with vehicle and atmospheric data measured during flight. The updates improved the simulation's prediction of the actual flight and aided in assessing the accuracy of its prediction. The available flight data allowed updates to the FTV mass properties, thrust, and atmospheric models. Specifically, the motor thrust profile was reconstructed from chamber pressure measurements, which were also used to generate mass flow rate vs. time used to estimate mass properties as a function of time. The post-flight simulation used the MET atmosphere model. These updates to mass properties, thrust, and atmosphere were implemented without dispersion due to lack of uncertainty models being provided with these updates. Additional detail on these simulations can be found in Ref. 16.

The following figures provide several comparisons between the pre-flight simulation, post-flight simulation, and the BET reconstructed from the flight data, over the ascent phase of flight. Other comparisons including stage separation and entry trajectory comparisons are provided in Reference 17.

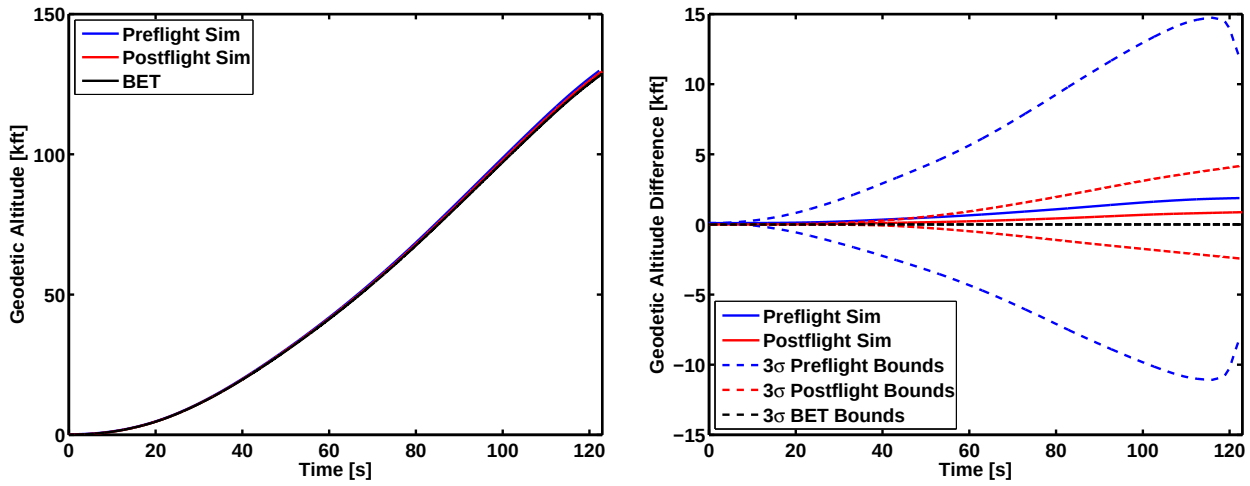

(a) Altitude

(b) Altitude Difference

Figure 13: Altitude Comparison

Figure 13(a) shows the geodetic altitude time history for the trajectories during the ascent phase of flight. Figure 13(b) shows the differences in the simulated time histories relative to the BET altitude. Additionally, the 3-σ bounds of the pre-flight and post-flight Monte-Carlo simulations along with the 3-σ bounds of the BET are shown. The figures show that the BET position throughout the powered ascent was within the predicted boundaries. Other position variables such as latitude and longitude show the same behavior.

Figure 14(a) shows the Mach number time history for the simulations and the BET. The differences relative to the BET Mach estimate are shown in Figure 14(b) along with the 3-σ boundaries. In both the pre-flight and post-flight simulations, the BET Mach number is well within the uncertainty envelope. Interestingly, the BET Mach uncertainty is initially much smaller than the post-flight simulation uncertainty but at a time of approximately 90 seconds the BET uncertainties grow larger than the simulation uncertainties. This behavior is due to the atmosphere (winds and speed of sound) not being dispersed in the post-flight simulation since no dispersion model was available. The BET uncertainty increases with altitude since the GRAM uncertainties are larger than the balloon-based MET uncertainties above 100 kft.

Figure 15(a) compares the dynamic pressure time history for the simulation cases and the BET. Here, the pre-flight simulation shows some noticeable differences relative to the BET, which are primarily due to the GRAM monthly mean atmosphere being used in the simulation. The post-flight simulation with

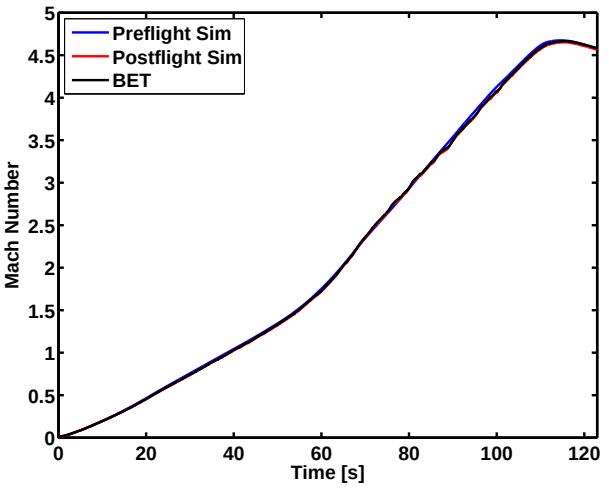

(a) Mach Number

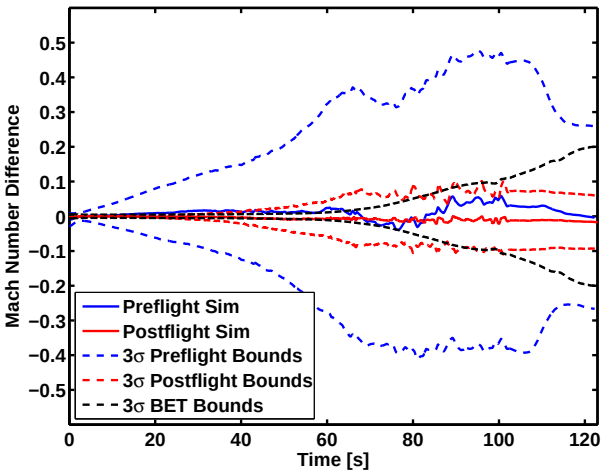

(b) Mach Number Difference

Figure 14: Mach Number Comparison

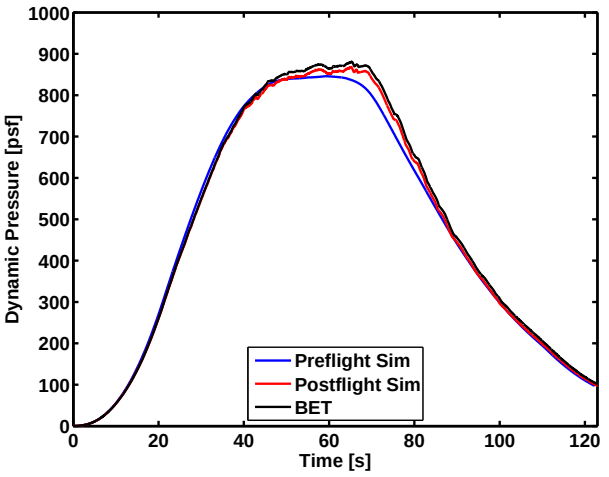

(a) Dynamic Pressure

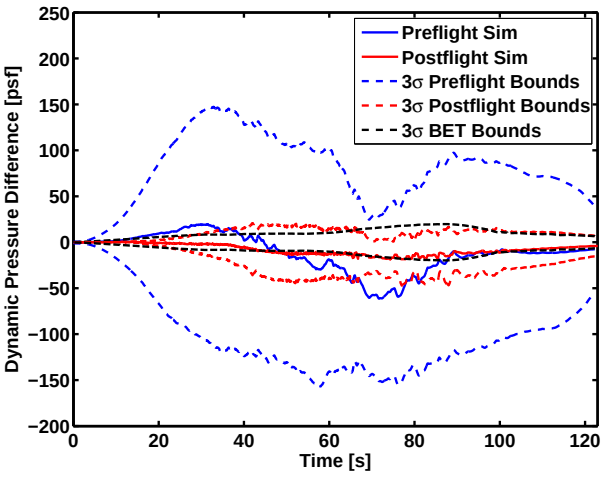

(b) Dynamic Pressure Difference

Figure 15: Dynamic Pressure Comparison

the measured MET profile shows a much better match to the BET. In both cases, the BET is within the uncertainty bounds of the Monte-Carlo simulations. Note that the post-flight simulation bounds are optimistic in the sense that the atmosphere is not dispersed in the simulation.

The wind-relative angle of attack time histories for the BET, and the pre-flight and post-flight simulations is shown in Figure 16(a) with differences relative to the BET shown in Figure 16(b). Similarly, the wind-relative angle of sideslip time histories and differences are shown in Figure 17(a) and (b), respectively. The pre-flight simulation results are considerably different than the post-flight and BET cases, primarily due to the updated atmospheric wind profile based on the MET data rather than the GRAM monthly mean profile. The post-flight simulation results appear to be slightly biased relative to the BET, particularly in the angle of attack. This behavior is due to the altitude profile being slightly different between the post-flight simulation and the BET so that the wind time history along the trajectory is shifted. In both simulation cases, the BET falls well within the 3-σ Monte-Carlo bounds, with the exception of the portion of the post-flight simulation trajectory within the first 20 seconds of flight. This effect arises due to the wind profile being held constant, which ordinarily would dominate the uncertainties in the region of flight with relatively low ground-relative velocity.

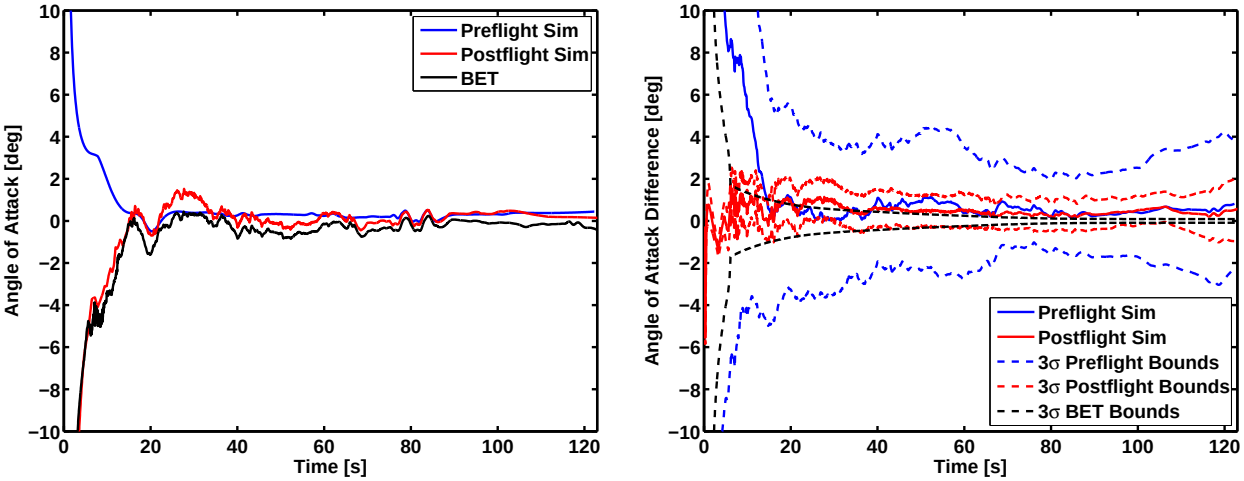

(a) Angle of Attack

(b) Angle of Attack Difference

Figure 16: Angle of Attack Comparison

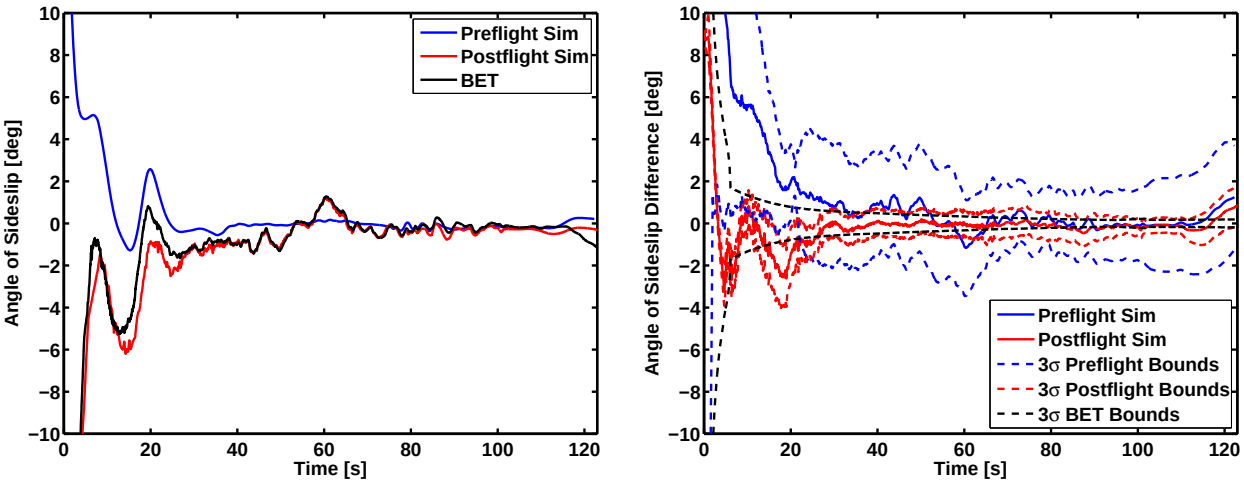

(a) Angle of Sideslip

(b) Angle of Sideslip Difference

Figure 17: Angle of Sideslip Comparison

SUMMARY AND CONCLUSIONS

This paper describes the approach and methodology employed to generate the Best Estimate of Trajectory (BET) for the Ares I-X test flight, which occurred on October 28th, 2009. The trajectory reconstruction process combines on-board, ground-based, and atmospheric measurements to produce the trajectory estimates, using an Iterative Extended Kalman Filter algorithm. This paper describes the methodology and results of the trajectory reconstruction process, including flight data preprocessing and input uncertainties, trajectory estimation algorithms, output transformations, and comparisons with preflight predictions.

ACKNOWLEDGEMENTS

The authors wish thank Stanley I. Adelfang, Robert E. Barbre, Thomas D. Bruchmiller, Eugene H. Heim, Frank B. Leahy, Roger X. Lenard, and Brady A. White for assistance with various data processing and uncertainty analysis activities in support of the Ares I-X BET.

REFERENCES

[1] Davis, S. R. and Askins, B. R., "Ares I-X: First Flight of a New Generation," American Institute of Aeronautics and Astronautics, AIAA Paper 2010-6910, July 2010.

[2] Campbell, J. F. and Brandon, J. M., "Calibration and Flight Test Results for the Ares I-X 5-Hole Probe," *Acta Astronautica*, Vol. 68, No. 7-8, 2011, pp. 1219–1227.

[3] Roberts, R. C., "Ares I-X Final Meteorological Profile," Ares I-X Transmittal Letter, MSFC Natural Environments Group, November 5, 2009.

[4] Wagner, W. E. and Serold, A. C., "Formulation on Statistical Trajectory Estimation Programs," NASA CR-1482, January 1970.

[5] Karlgaard, C. D., Tartabini, P. V., Blanchard, R. C., Kirsch, M., and Toniolo, M. D., "Hyper-X Post-Flight Trajectory Reconstruction," *Journal of Spacecraft and Rockets*, Vol. 43, No. 1, 2006, pp. 105-115.

[6] Karlgaard, C. D., Tartabini, P. V., Martin, J. G., Blanchard, R. C., Kirsch, M., Toniolo, M. D., and Thornblom, M. N., "Statistical Estimation Methods for Trajectory Reconstruction: Application to Hyper-X," NASA TM-2009-215792, August 2009.

[7] Fraser, D. C. and Potter, J. E., "The Optimum Linear Smoother as a Combination of Two Optimum Linear Filters," *IEEE Transactions on Automatic Control*, Vol. 14, No. 8, 1969, pp. 387–390.

[8] Crassidis, J. L. and Junkins, J. L., *Optimal Estimation of Dynamic Systems*, Chapman & Hall/CRC, Boca Raton, FL, 2004.

[9] Vallado, D. A., *Fundamentals of Astrodynamics and Applications,* McGraw-Hill, New York, 1997, pp. 20-27.

[10] Sofair, I., "Improved Method for Calculating Exact Geodetic Latitude and Altitude Revisited," *Journal of Guidance, Control, and Dynamics*, Vol. 23, No. 2, 2000, p. 369.

[11] Minzer, R. A., Reber, L. G., Jacchia, L. G., Huang, F. T., Cole, A. E., Kantor, A. J., Kenesha, T. J., Zimmerman, S. P., and Forbes, J. M., "Defining Constants, Equations, and Abbreviated Tables of the 1975 U.S. Standard Atmosphere," NASA TR R-459, May 1976.

[12] "IERS Bulletin B 262," http://data.iers.org/products/207/13077/orig/bulletinb-262.txt

[13] McCarthy D. D. and Petit, G., "IERS Conventions (2003)," IERS Technical Note No. 32, 2004.

[14] Nørgaard, M., Poulsen, N. K., and Ravn, O., "New Developments in State Estimation for Nonlinear Systems," *Automatica*, Vol. 36, No. 11, 2000, pp. 1627-1638.

[15] Lear, W. M., "The Ascent/Entry BET Program, LRBET5," JSC-19310, Mission Planning and Analysis Division, NASA Johnson Space Center, December 1983.

[16] Starr, B. R., Olds, A. D., and Craig, A. S., "Ares I-X Range Safety Three Sigma Trajectory Envelope Analysis," 58th JANNAF Propulsion Meeting, April 2011.

[17] Karlgaard, C. D., *et al*, "Ares I-X Best Estimated Trajectory and Comparisons with Preflight Predictions," American Institute of Aeronautics and Astronautics, AIAA Atmospheric Flight Mechanics Conference, Portland, OR, August 2011, to appear.